1

Ion Spectroscopy and Guided Ion Beam Studies of Protonated Asparaginyl-Threonine

Decomposition: Influence of a Hydroxyl Containing C-Terminal Residue on Deamidation

Processes

Georgia C. Boles, Lisanne J. M. Kempkes, Jonathan Martens, Giel Berden, Jos Oomens, J. S.

P. B. Armentrout^{†,*}

[†] Department of Chemistry, University of Utah, 315 S. 1400 E. Rm. 2020, Salt Lake City, Utah

84112, United States

‡Radboud University, Institute for Molecules and Materials, FELIX Laboratory, Toernooiveld 7,

6525 ED, Nijmegen, The Netherlands

§ Van't Hoff Institute for Molecular Sciences, University of Amsterdam, Science Park 904,

NL-1098 XH Amsterdam, The Netherlands

Keywords: thermochemistry; spectroscopy; deamidation; collision-induced dissociation

Abstract

The spontaneous deamidation of asparagine residues plays a significant role in various biological

functions and degenerative, aging diseases. Here, we present a full description of the deamidation

reaction (as well as other key dissociation processes) of protonated asparaginyl-threonine,

[AsnThr+H]⁺, via complementary infrared multiple photon dissociation (IRMPD) ion

spectroscopy, threshold collision-induced dissociation (TCID), and theoretical studies. IRMPD

spectra allow for the clear identification of precursor and product ion structural conformations

when compared to theoretically calculated spectra for likely structures. Analysis of kinetic energy

dependent cross sections measured via TCID with xenon using a guided ion beam tandem mass

spectrometer allows for characterization of the energies involved in the decomposition processes

of interest. Threshold energies are compared to relative single point energies of major reaction

species calculated at B3LYP, B3LYP-GD3BJ, B3P86, and MP2(full) levels of theory, thereby determining important rate-limiting steps involved in [AsnThr+H]⁺ decomposition. Our studies confirm the formation of a succinimide intermediate via deamidation of [AsnThr+H]⁺, an observation consistent with condensed-phase deamidation analyses. Interestingly, our spectroscopic results suggest deamidation does not produce furanone isomers even though theoretical results indicate this pathway (exhibited in gas-phase analyses of similar dipeptide systems) should be competitive. Dehydration of [AsnThr+H]⁺ is also observed, where theory suggests that oxazolone and oxazoline formation are competitive at threshold energies, but IRMPD analyses conclusively confirm the formation of the oxazoline structure. The comprehensive results presented (in addition to complementary studies discussed herein) allow for a valuable analysis of C-terminal residue side-chain effects on the deamidation process.

Introduction

Deamidation of asparaginyl (Asn) residues, a spontaneous degradation pathway influencing a wide range of biologically important functions, [1-4] has been the focus of numerous experimental [1, 2, 4-11] and theoretical [12-15] studies. Although succinimide (Suc) formation, followed by hydrolysis to form aspartate (Asp) and iso-aspartate (iso-Asp), is a widely accepted pathway for protein deamidation, diverse reaction mechanisms have been proposed for these processes [7, 12, 15, 16]. Because transient succinimide reaction products are difficult to observe experimentally, ascertaining information about key elementary steps in solution is problematic and limits the availability of complete reaction mechanisms. Nevertheless, these experimental analyses have provided valuable information regarding how deamidation rates are affected by primary [1, 17], secondary [18], tertiary [19], and quaternary [20] protein structure. In particular, analyses of neighboring n+1 residues (where n=1 Asn) have indicated that the primary protein structure greatly influences deamidation rates. For example, for n+1 residues of glycine (Gly), alanine (Ala), threonine (Thr), and valine (Val), deamidation halftimes were found to be 1.2, 25, 47, and 253 days, respectively [1]. Clearly, the enhanced deamidation of -1

given the absence of steric hindrance and side-chain hydrogen bonding introduced by the glycyl side chain during succinimide formation. However, the drastically different deamidation rates of —AsnThr— and —AsnVal— are unexplained on the basis of steric effects alone, suggesting that side-chain functionality also plays a role in the reaction. This effect could be a consequence of the side-chain dipole, hydrogen bonding, or both.

Thus, the current work presents a full description of the [AsnThr+H]⁺ deamidation process using threshold collision-induced dissociation (TCID) carried out in a guided ion beam tandem mass spectrometer (GIBMS) in order to evaluate the energetics of this process. In addition to succinimide analogues, alternative cyclic structures (e.g., furanone, Fur) can be formed via deamidation processes [8-11], an observation not commonly reported in condensed phase media [3]. Therefore, complementary ion spectroscopy studies via infrared multiple photon dissociation (IRMPD) have been completed, allowing for the unambiguous structural identification of the deamidation and dehydration products observed (an aspect for which TCID studies can be less definitive). IRMPD spectroscopy has proven to be a valuable tool to distinguish isomers, tautomers, and conformers in the structural determination of precursor and MSⁿ fragment ions [21-30].

Our groups have previously evaluated the deamidation processes of prototypical asparginyl dipeptides with n+1 residues of Gly [8], Ala [9, 11], and Val [10], such that the comparison to the current [AsnThr+H]⁺ system should allow for valuable insight regarding the energetic and mechanistic contributions of a functionalized side chain to the deamidation processes. In particular, these previous studies indicated that deamidation of [AsnGly+H]⁺ leads to a Suc structure at threshold energies, with contribution from the Fur product at higher energies [8]. Deamidation of [AsnAla+H]⁺ follows a bifurcating mechanism resulting in the observation of both Fur and Suc structures [9, 11], and deamidation of [AsnVal+H]⁺ forms only a Fur structure [10]. On this basis, it is interesting to evaluate the effect of side-chain functionality in the current [AsnThr+H]⁺ system, as compared to the aliphatic side chains studied previously.

In the present work, both IRMPD and TCID experimental analyses are reported in parallel with complete quantum-chemical calculations, where key reaction energies are reported at the B3LYP, B3LYP-GD3BJ, B3P86, and MP2(full) levels of theory. This comprehensive analysis evaluates the deamidation pathway of [AsnThr+H]⁺, as well as dehydration and other key dissociation channels. More importantly, the comprehensive analysis of all above-mentioned systems reveals insight into the deamidation processes in the gas phase, as well as how these results can be correlated to condensed-phase findings.

Experimental and Computational Section

General Experimental Procedures – IRMPD Spectroscopy

IRMPD spectra of precursor [AsnThr+H]⁺ ions, its [AsnThr+H–NH₃]⁺ deamidation product, its [AsnThr+H–H₂O]⁺ dehydration product, and its subsequent [AsnThr+H–NH₃–H₂O]⁺ fragment were measured using infrared light generated by the FELIX free electron laser [31]. A modified 3D quadrupole ion trap mass spectrometer (Bruker, AmaZon Speed ETD, Bremen, Germany) [32] coupled to the FELIX beamline was used. The protonated precursor dipeptide was generated via electrospray ionization (ESI), where AsnThr (purchased from Biomatik, Canada) was dissolved in a 50:50 acetonitrile:water solution at a concentration of 10⁻⁶ M with ~1% formic acid added to enhance protonation. The [AsnThr+H-NH₃]⁺, [AsnThr+H-H₂O]⁺, and [AsnThr+H-NH₃-H₂O₁⁺ fragments were produced by low-energy collisional activation with helium for 40 ms with an amplitude parameter of approximately 0.3 V. The IRMPD spectrum of the precursor ion was measured over the 1000 – 1800 cm⁻¹ range and those for the fragment ions were measured from 1000 to 2000 cm⁻¹. At each wavelength, the ions were irradiated by two FELIX pulses at a repetition rate of 10 Hz with a pulse energy between 5 and 50 mJ. The bandwidth of the FELIX radiation is about 0.5% of the center frequency. IRMPD spectra were generated by determining the dissociation yield at every wavelength via $\sum I(fragment ions) / \sum I(fragment ions +$ precursor ion), where I is the ion intensity [33]. The yield was determined from five averaged mass spectra and was corrected linearly for the frequency dependent pulse energy.

General Experimental Procedures – GIBMS

Kinetic energy dependent cross sections for the TCID of [AsnThr+H]⁺ with xenon (Xe) were measured using a GIBMS that has been described in detail elsewhere [34-36]. Briefly, ions were generated using an ESI source under similar conditions to those described previously [37]. The ESI was operated using 10⁻⁴ M AsnThr (purchased from Biomatik, Canada) in 50:50 methanol:water solution with the addition of 0.1% acetic acid (purchased from Sigma-Aldrich, St. Louis, MO, USA). (Here, the concentration of dipeptide needed is higher than in the IRMPD studies in order to obtain sufficient intensity for the more demanding ion beam experiments. Differing acid concentrations are arbitrary as the samples are easily protonated; but in both cases, freshly made solutions were used to avoid sample degradation prior to use.) This solution was syringe-pumped at a rate of 50 μ L/hr into a 35 gauge stainless steel needle biased at 2000 – 2400 V relative to ground. Ions were directed through a heated capillary at 80 °C into a radio frequency (rf) ion funnel [38], where they were focused into a tight beam. After exiting the ion funnel, the ions entered an rf trapping hexapole ion guide where they underwent on the order of 10⁴ thermalizing collisions with ambient gas [37]. As demonstrated in earlier studies, ions produced in the source region should have a Maxwell-Boltzmann distribution of rovibrational states at 300 K [37, 39-42].

Precursor ions were extracted from the source and mass selected using a magnetic momentum analyzer, decelerated to a well-defined kinetic energy, and focused into an rf octopole ion guide that trapped the ions radially [43, 44], which minimized losses of product and reactant ions. The ions then passed through a collision cell containing Xe [45, 46] at a pressure ≤ 0.3 mTorr. At these pressures, the number of ions undergoing single collisions was sufficient to form product ions characterized by a high intensity, while minimizing the opportunity for multiple collisions to occur. The product and residual reactant ions drifted to the end of the octopole guide, where they were extracted and focused into a quadrupole mass filter (operated under conditions that ensured unit mass resolution while maintaining efficient transmission) for mass analysis. Ions were detected with a high voltage dynode and scintillation detector [47], and the signal was processed

using standard pulse counting techniques. Ion intensities of reactants and products, measured as a function of collision energy, were converted to absolute cross sections as described previously [34]. Briefly, the calculation of the reaction cross section, σ_{tot} , from the ion intensities utilized a relationship that is directly analogous to the Beer-Lambert law, specifically, $I = I_0 \exp(-\rho \sigma_{tot} l)$, where I is the reactant ion intensity after passing through the collision cell, I_0 is the reactant ion intensity entering the collision cell and equals $I + \sum I_j$ (where I_j = intensity of a product ion in channel i), l is the effective length of the collision cell (8.3 cm) [34], and ρ is the number density of the neutral reactant and equals P/k_BT , where P and T are the pressure and temperature of the gas and k_B is Boltzmann's constant. Reaction cross sections for individual product ions are given by $\sigma_j = \sigma_{\text{tot}} (I_j / \sum I_j)$. The uncertainty in these relative cross sections is about $\pm 5\%$ and that for the absolute cross sections is about $\pm 20\%$. The ion kinetic energy distribution was measured using a retarding potential analysis and found to be Gaussian with a typical full width at half maximum (FWHM) of 0.1 - 0.2 eV (lab). Uncertainties in the absolute energy scale were about ± 0.05 eV (lab). Ion kinetic energies in the laboratory (lab) frame were converted to energies in the centerof-mass (CM) frame using $E_{CM} = E_{lab} \times m/(m+M)$, where M and m are the masses of the ionic and neutral reactants, respectively. All energies in this work are reported in the CM frame unless stated otherwise.

Thermochemical Analysis

Threshold regions of the CID cross sections were modeled using eq 1,

$$\sigma_{j}(E) = \left(n\sigma_{0,j}/E\right) \sum_{i} g_{i} \int_{E_{0,j}-E_{i}}^{E} \left[k_{j}(E^{*})/k_{tot}(E^{*})\right] \left\{1 - e^{-k_{tot}(E^{*})\tau}\right\} (E - \varepsilon)^{n-1} d(\varepsilon)$$
 (1)

where $\sigma_{0,j}$ is an energy-independent scaling factor for channel j, n is an adjustable, empirical representation of factors that describe the efficiency of the energy transfer during the collision and varies with the complexity of the system being studied [35], E is the relative kinetic energy of the reactants, $E_{0,j}$ is the threshold for dissociation of the ground electronic and rovibrational state of the reactant ion at 0 K for channel j, τ is the experimental time available for dissociation (\sim 5 × 10^{-4} s, as measured by previous time-of-flight studies) [35], ε is the energy transferred during the

collision, and E^* is the internal energy of the energized molecule (EM) after the collision, so that $E^* = \varepsilon + E_i$. The summation is over the rovibrational states of the reactant ions, i, where E_i is the excitation energy of each state and g_i is the fractional population of those states ($\Sigma g_i = 1$). The Beyer–Swinehart-Stein-Rabinovitch algorithm [48-50] was used to evaluate the number and density of the rovibrational states and the relative populations g_i were calculated for a Maxwell-Boltzmann distribution at 300 K. The term $k_j(E^*)$ is the unimolecular rate constant for dissociation of the EM to channel j via its rate-limiting transition state (TS). The rate constants $k_j(E^*)$ and $k_{tot}(E^*)$ are defined by Rice-Ramsperger-Kassel-Marcus (RRKM) theory [51, 52] as in eq 2,

$$k_{tot}(E^*) = \sum_{j} k_j(E^*) = \sum_{j} s_j N_j^{\dagger}(E^* - E_{0,j}) / h\rho(E^*)$$
 (2)

where s_j is the reaction degeneracy of channel j, $N_j{}^{\dagger}(E^* - E_{0,j})$ is the sum of rovibrational states for the TS of channel j at an energy $E^* - E_{0,j}$, and $\rho(E^*)$ is the density of states of the EM at the available energy, E^* . These rate constants allow both kinetic shifts (where the probability of dissociation is given by the term $\{1 - e^{-k_{tot}(E^*)\tau}\}$ in eq 1) and competition between multiple channels (which is controlled by the ratio of rate constants in eq 1, $[k_j(E^*)/k_{tot}(E^*)]$) to be modeled accurately [53, 54].

To evaluate the rate constants in eqs 1 and 2, values for rovibrational energies for the EM and the rate-limiting TSs were determined from quantum-chemical calculations described below. Additionally, the entropy of activation at 1000 K for each dissociation channel, $\Delta S^{\dagger}_{1000}$, was calculated as described in detail elsewhere [53]. The model cross sections of eq 1 were convoluted with the kinetic energy distributions of the reactants [34] and compared to the experimental data. A nonlinear least-squares analysis was used to provide optimized values for $\sigma_{0,j}$, n, and $E_{0,j}$. The uncertainty in $E_{0,j}$ (reported as one standard deviation) was estimated from the range of threshold values determined from multiple sets of data, variations in the parameter n ($\pm 10\%$ around the optimum value), variations in vibrational frequencies ($\pm 10\%$), changes in τ by factors of 2, and the uncertainty in the absolute energy scale. Uncertainties associated with variations in the

vibrational frequencies that control the internal energy and the kinetic shifts were assessed independently.

Computational Details

Ground structures (GS) of reactant and product species of interest were located using the Gaussian 09 suite of programs [55]. Structures analogous to those reported previously for [AsnGly+H]⁺ [8], [AsnAla+H]⁺ [11], and [AsnVal+H]⁺ [10], were used as starting structures and further optimized at both the B3LYP and B3LYP-GD3BJ/6-311+G(d,p) levels, where GD3BJ indicates the use of empirical dispersion corrections using the D3 version of Grimme's dispersion with Becke-Johnson damping [56]. Additional key reaction intermediates and all TSs were also initially taken from the structures reported in previous studies and were optimized at the same levels of theory. Rotational constants and vibrational frequencies were calculated from optimized structures, and vibrational frequencies were scaled by a factor of 0.989 [57] when used for the determination of internal energy, RRKM calculations, and zero-point vibrational energy (ZPE) corrections. Single point energies were calculated at the B3LYP, B3P86, and MP2(full) levels using the 6-311+G(2d,2p) basis set and B3LYP geometries, and at the B3LYP-GD3BJ/6-311+G(2d,2p) level using B3LYP-GD3BJ geometries. For spectral comparisons, IR spectra were calculated from B3LYP/6-311+G(d,p) optimized structures, where computed harmonic vibrational frequencies were scaled by 0.975 [9, 10, 29, 30] and convoluted with a 25 cm⁻¹ FWHM Gaussian line shape to facilitate comparison with experimental spectra.

Results

Theoretical Results for Low-Energy Conformers and IRMPD Spectrum of [AsnThr+H]+

Several low-energy conformations of $[AsnThr+H]^+$ were located, with key species and their 298 K relative Gibbs energies shown in Figure 1. Conformers are named according to their protonation sites (including additional hydrogen bonds) by using the designation [X,Y,Z] where X = protonated atom and Y,Z = site of hydrogen bonds in the order of increasing hydrogen bond length. The protonation site is followed by the series of dihedral angles starting from the

N-terminal side-chain amide group nitrogen to the C-terminal carboxylic acid. Backbone nitrogen and oxygen atoms are numbered by residue along the backbone chain starting from the N-terminus and the hydroxyl oxygen is labeled O^3 . Side-chain nitrogen and oxygen atoms are designated by a superscript s and are numbered by residue. (An overview of this nomenclature used is given in Figure 1.) Dihedral angles are distinguished as c (cis, for angles between $0^\circ - 45^\circ$), g (gauche, $45^\circ - 135^\circ$), or t (trans, $135^\circ - 180^\circ$).

The two lowest energy conformers, [N¹,CO¹s,CO¹]-ttgtgtt (predicted to be the 0 K GS at the B3LYP level of theory) and [N¹,CO¹s,CO¹]-gggtgtt (predicted to be the 0 K GS at the B3LYP-GD3BJ, B3P86, and MP2(full) levels of theory) were found to be within 4 kJ/mol of each other, similar to relative energies observed for analogous [AsnGly+H]+ [8], [AsnAla+H]+ [11], and [AsnVal+H]+ [10] systems. At 298 K, the former conformation is the GS at all levels except MP2, but they remain within 4 kJ/mol of one another. These two conformers are distinguished by a head-to-tail hydrogen bonding N¹sH•O²C interaction in gggtgtt, which is absent in ttgtgtt. Notably, both conformers exhibit hydrogen bonding between the peptide bond nitrogen and the side-chain Thr hydroxyl oxygen (N²H•O²sH) rather than to the carbonyl oxygen (N²H•O²C), the motif observed in the GSs of the previously studied protonated aliphatic side chain AsnXxx systems (Xxx = Gly [8], Ala [9, 11], and Val [10]). The lowest energy conformer having this latter hydrogen bond, [N¹,CO¹s,CO¹]-ttgtttt (shown in Figure 1), is located 14 – 23 kJ/mol above the predicted GSs at 0 K (12 – 18 kJ/mol at 298 K). Hence, a direct comparison of the relative energies between the current system and the aliphatic systems is not appropriate, as discussed further below.

Figure 1 also displays the experimental IRMPD spectrum of [AsnThr+H]⁺ together with the calculated spectra of the aforementioned low-energy conformers. Major spectral features of the [AsnThr+H]⁺ IRMPD spectrum are located at 1768, 1715, 1608, 1519, 1402, and 1131 cm⁻¹. These features are reproduced well by the calculated spectrum for the [N¹,CO^{1s},CO¹]-ttgtgtt species, which has predicted bands centered at 1767 (backbone CO² stretch), 1697 (peptide bond CO¹ stretch at 1708 cm⁻¹ along with amide CO^{1s} stretch at 1683 cm⁻¹), 1607 (amino N¹H₃ rock and wag as well as contributions from the amide N^{1s}H₂ bend), 1515 (N²H wag), 1398 and 1411 (amino

N¹H₃ umbrella and CN^{1s}H bend along with minor contributions from CH₂ and CH₃ motions), 1346 (CH motions along the backbone and CO³H bend), 1148 (backbone CO³H bend), and 1098 cm⁻¹ (delocalized distortions along the backbone and side chain). This theoretical spectrum fails to predict appreciable intensity at 1450 cm⁻¹, whereas a shoulder is clearly visible in the experimental spectrum.

Similar spectral features are observed in the higher energy [N¹,CO^{1s},CO¹]-ttgtttt conformer, although the two high frequency CO stretch bands are red shifted compared to the experimental bands, and the bands centered at 1063 cm⁻¹ no longer lie within the experimental envelope. In this species, the local environment of the CO² stretch is now affected by the N²H•O²C hydrogen bond. Likewise, a similar shift of the highest frequency band is observed in the gggtgtt species, which is characterized by an N^{1s}H•O²C hydrogen bond. Additionally, the intense NH₃ umbrella motion exhibited by this species is predicted at 1473 cm⁻¹, a 70 cm⁻¹ shift from the comparable band of ttgtgtt. Some contribution from this band could explain the intensity observed in this region as a side band, as well as the enhanced intensity to the red of the experimental band centered at 1402 cm⁻¹. Thus, we conclude that the major species observed is the [N¹,CO^{1s},CO¹]ttgtgtt conformer, with minor contributions from the gggtgtt species, consistent with its low relative energy. Although the ttgtttt species reproduces the experimental spectrum in many respects fairly well, it is not needed to reproduce the experimental spectrum and its relatively high energy suggests the probability of forming this conformer is low. On the basis of an equilibrium distribution of conformers at 298 K, its population should be < 0.4% at all levels of theory; whereas the populations of the ttgtgtt/gggtgtt conformers should be 77/14, 52/46, and 68/25% at the B3LYP, B3LYP-GD3BJ, and B3P86 levels of theory, respectively. The MP2 level instead inverts the relative populations at 43/52%.

Cross Sections for Collision-Induced Dissociation of [AsnThr+H]+

Experimental kinetic energy dependent cross sections were measured for the interaction of Xe and [AsnThr+H]⁺ under unit mass resolution conditions, with efficient product ion transmission as demonstrated previously [8, 10, 11]. Figure 2 shows a representative data set measured at 0.3

mTorr of Xe, where eight product channels are observed and described in Scheme 1. Scheme 1 only depicts the lowest energy pathways found for these decomposition processes. In some cases, higher energy pathways are also discussed in the text below.

The product channel with the lowest threshold energy results from dehydration of the dipeptide (leading to the formation of m/z 216). Dehydration pathways leading to protonated oxazolone, [OxaO+H]⁺, and oxazoline structures, [OxaI+H]⁺, were located. Competitively, deamidation (m/z 217) is observed starting at energies ~0.4 eV higher. Here, Suc, Fur, and diketomorpholine (DKM) structures (as shown in Scheme 2) are isobaric such that pathways leading to these protonated [Suc+H]⁺, [Fur+H]⁺, and [DKM+H]⁺ structures were all explored. [AsnThr+H]⁺ can also dissociate via cleavage of the peptide bond with accompanying elimination of CO (formation of m/z 87, identified as $[APA+H]^+$, where APA = 3-aminopropanamide, along with Thr + CO) or without CO-loss (formation of m/z 120, [Thr+H]⁺, along with 1-oxa-3,5-aminocyclopentan-2-one, OACP). Here, these processes have apparent onsets at about 2.3 eV and 2.0 eV, respectively. At higher energies, the competitive formation of m/z 130, 199, and 200 is observed. Scheme 1 identifies the former channel as cleavage of the peptide bond in the m/z 216 [OxaO+H]⁺ product ion (loss of APA), and the latter two channels as sequential losses of H₂O and NH₃ from m/z 217, respectively. As discussed below, a competitive pathway leading to m/z 199 by deamidation of the [OxaI+H]⁺ dehydration product, a possibility shown in Scheme 1, was also located. Here, two different m/z 199 bicyclic structures are predicted. At even higher energies, the formation of m/z 175 (asparaginyl side chain loss from [AsnThr+H]⁺ to form [GlyThr+H]⁺) is observed with low intensity. These high energy, small magnitude cross sections were difficult to measure at lower pressures. Therefore, modeling of these channels to acquire thermodynamic information was not possible.

Theoretical Results for Deamidation Pathways

Two competitive pathways, leading to either succinimide or furanone formation, were located for the deamidation of [AsnThr+H]⁺. In previous work for [AsnGly+H]⁺, complete pathways for deamidation (as well as other decomposition reactions) were elucidated

computationally [8]. As the present pathways should be comparable, we focus here on just the product and rate-limiting TSs for each process of interest. Relative energies of these major reaction species for both pathways are given in Table 1. The rate-limiting step for furanone formation occurs via a pathway analogous to that observed previously [8, 10, 11], see Figure 3. In this mechanism, proton transfer from N¹ to N^{1s} results in the formation of the NH₃ leaving group. Then, C-NH₃ bond elongation in the following step results in concerted motions of C-NH₃ bond rupture and furanone ring formation over a tight TS_{N-Fur}, which B3LYP and B3P86 suggest is rate limiting. This process yields [Fur+H]+-3.1 (protonation at site 3, Scheme 2), which the B3LYP-GD3BJ and MP2 levels of theory predict is the rate-limiting step (by 17.5 and 9.0 kJ/mol, respectively). For succinimide formation (Figure 3), the precursor to the rate-limiting step is characterized by proton transfer from N² to N^{1s}, yielding the NH₃ leaving group. A subsequent decrease in the distance between the side-chain carbon and the peptide bond nitrogen (N²) initiates cyclization, which occurs in the rate-limiting step via TS_{N-Suc} (127 – 150 kJ/mol above the GS). As shown in Figure 3, this pathway yields a protonated succinimide structure, [Suc+H]+-1.2 (protonation at site 1, Scheme 2). This product channel lies 16 – 30 kJ/mol below TS_{N-Suc}, such that the latter is ratelimiting at all levels of theory. Overall, B3LYP-GD3BJ, B3P86, and MP2 place TS_{N-Suc} below the rate-limiting step for Fur formation (by 4 - 16 kJ/mol), whereas B3LYP suggests the opposite (by 13 kJ/mol).

Table 2 shows an exploration of possible protonation sites (as identified in Scheme 2) for [Suc+H]⁺, [Fur+H]⁺, and [DKM+H]⁺ structures (where the latter results from deamination rather than deamidation of the precursor ion). For the [Suc+H]⁺ structures, the MP2 level of theory suggests that protonation at site 1 (N¹) is lowest in energy among all possible structures. Exploration of conformational space resulted in the location of several [Suc+H]⁺-1 structures, as shown in Table 3, Figure 3, and Supporting Information Figure S1. [Suc+H]⁺-1.1 contains a N¹H•O²C hydrogen bond (Figure S1) and is lowest in energy at 0 K at all levels of theory and at the B3LYP-GD3BJ and B3P86 levels at 298 K. [Suc+H]⁺-1.2 (Figure 3) and 1.3 (Figure S1) exhibit N¹H•O²sH and N¹H•O¹C hydrogen bonds, respectively, where the latter is formed between

the N¹ site and the adjacent carbonyl oxygen of the succinimide ring. The N¹H•O²C interaction in 1.1 is broken in the 1.2 and 1.3 structures because of rotation around the ∠CNCC dihedral angle. This rotation is favorable entropically considering Gibbs energies, where the 1.2 and 1.3 structures are the MP2 and B3LYP 298 K GSs, respectively. At 0 K, these structures are located within 0.3 − 6 and 5 − 14 kJ/mol of [Suc+H]+-1.1. Interestingly, B3LYP and B3P86 levels of theory suggest that the lowest energy [Suc+H]+ structure is protonated at site 4 (by 8 and 7 kJ/mol), see Table 2, which is stabilized through a hydrogen bond with the side-chain hydroxyl group. The 0 K B3LYP reaction coordinate leading to this structure (from [Suc+H]+-1.1) is given in Supporting Information Figure S2, where the proton transfer from site 1 to site 4 (passing through a [Suc+H]+-5 TS) requires 197 − 205 kJ/mol, 51 − 70 kJ/mol higher in energy than TS_{N-Suc}. Therefore, even if [Suc+H]+-4.1 is lower in energy than [Suc+H]+-1.1, it is not likely to participate in the deamidation process. Nonetheless, different conformers of [Suc+H]+-4 were explored, as shown in Figure S3.

For the [Fur+H]⁺ structures, all levels of theory agree that [Fur+H]⁺-3.1 is lowest in energy, see Tables 2 and 3, where protonation at the imide nitrogen is stabilized by N²H•O^{2s}H and N²H•N¹H₂ hydrogen bonds (Figure 3). Higher energy [Fur+H]⁺-3.2, 3.3, and 3.4 structures (see Supporting Information Figure S4) have 0 K relative energies 22 – 25, 29 – 31, and 36 – 37 kJ/mol above [Fur+H]⁺-3.1, respectively. Here, [Fur+H]⁺-3.2 rotates the Thr moiety to break the N²H•O^{2s}H hydrogen bond and replace it with a hydrogen bond at the O² carbonyl oxygen, N²H•O²C. 3.3 has neither of these but retains the N²H•N¹H₂ bond, whereas [Fur+H]⁺-3.4 maintains the N²H•O²C interaction while rotating the amino group to break the N²H•N¹H₂ bond.

The lowest energy [DKM+H]⁺ structure puts the proton on site 3, Scheme 2. Here, an exploration of conformational space results in the location of fewer structures compared to [Suc+H]⁺-1 and [Fur+H]⁺-3 structures because of the larger ring size. The lowest energy [DKM+H]⁺ structure of this type, [DKM+H]⁺-3.1 (Figure S5, 20 – 38 kJ/mol *lower* in energy than [Suc+H]⁺-1.1 at the B3LYP, B3LYP-GD3BJ, and B3P86 levels, and 6 kJ/mol *higher* in energy than [Suc+H]⁺-1.1 at the MP2 level) is stabilized by CO³H•O^{1s}C and N²H•O^{2s} H bonds.

[DKM+H]⁺-3.2 (Figure S5) maintains the latter hydrogen bond, but rotation of the asparaginyl side-chain amide group results in the formation of a CO³H•N^{1s}H₂ bond instead. This rotation results in an increase of 80 – 91 kJ/mol. It is also noteworthy that reaction mechanisms leading to [DKM+H]⁺ formation were explored, but none are competitive with those for [Suc+H]⁺ or [Fur+H]⁺ formation. The lowest energy DKM pathway located has a rate-limiting step lying 99 – 106 kJ/mol higher in energy than that for succinimide formation.

IRMPD Spectrum of [AsnThr+H-NH₃]⁺

Figure 4 shows the experimental IRMPD spectrum of [AsnThr+H-NH₃]⁺, with major spectral features located at 1840, 1790, 1745, 1581, 1390, and 1145 cm⁻¹. Here, most spectral features are consistent with succinimide formation, with the calculated spectra of [Suc+H]⁺-1.2, 1.3, and 1.5 reproducing the higher frequency features well. Each of these species exhibit three bands in the 1700 – 1900 cm⁻¹ region that correspond well with the experimental bands at 1840, 1790, and 1745 cm⁻¹. In particular, [Suc+H]⁺-1.2, 1.3, and 1.5 are characterized by bands at 1827, 1834, and 1837 cm⁻¹ (symmetric succinimide CO stretch), 1786, 1776, and 1792 cm⁻¹ (CO stretch of the carboxylic acid), and 1756, 1747, and 1746 cm⁻¹ (primarily asymmetric succinimide CO stretch, with additional contributions from N¹H₃ bend), which all exhibit deviations less than 15 cm⁻¹ from the experimental frequencies. Modest agreement is observed in the lower frequency region, where notably, the intense band at 1145 cm⁻¹ is not reproduced particularly well by any of the low-energy [Suc+H]⁺ product ions. Instead, [Suc+H]⁺-1.2, 1.3, and 1.5 each display overlapping bands at 1149 (COH bend) and 1166 (primarily CH distortions), 1146 and 1171, and 1148 and 1162 cm⁻¹, respectively. Further, each of the low-energy conformers exhibits a predicted band in the 1450 – 1500 cm⁻¹ region, for which there is only minor experimental evidence. [Suc+H]⁺-1.2 (the 298 K MP2 GS) is characterized by a band in this region shifted to slightly higher frequencies, 1505 cm⁻¹ (NH₃ umbrella), and modest intensity. [Suc+H]+-1.3 (the 298 K B3LYP GS) and 1.5, both exhibit more intense bands near 1455 cm⁻¹. The broad band observed at 1581 cm⁻¹ is also not reproduced by any of the [Suc+H]⁺ species, although each has less intense bands in this region.

The calculated spectrum of [Suc+H]⁺-1.1 is also given in Figure 4, where the shoulder observed at 1700 cm⁻¹ (concerted CO stretch of carboxylic acid and amino NH₃ distortions) could indicate its presence, as [Suc+H]⁺-1.2, 1.3, and 1.5 do not exhibit any spectral features in this region. The intense high-frequency band at 1756 cm⁻¹ (asymmetric CO stretches of succinimide ring) is centered between the 1790 and 1745 cm⁻¹ experimental bands, which suggests that this species is not a major contributor to the experimental spectrum. Most of the less intense bands are predominantly observed within experimental envelopes. Thus, contribution from [Suc+H]⁺-1.1 cannot be ruled out, although the spectral evidence suggests that a mixture of [Suc+H]⁺-1.2, 1.3, and 1.5 likely dominates.

Also given in Figure 4 is the comparison between the calculated spectrum of the [Fur+H]⁺-3.1 structure and the [AsnThr+H–NH₃]⁺ IRMPD spectrum. This conformer fails to reproduce the diagnostic high-frequency region. In particular, the experimental spectrum does not exhibit a band commensurate with the 1950 cm⁻¹ furanone CO stretching band, although there is potentially a very small absorption in this range. Additionally, this conformer does not reproduce the 1840 and 1745 cm⁻¹ bands that are reproduced in the calculated [Suc+H]⁺-1.2, 1.3, and 1.5 spectra. Further, none of the spectra for other Fur conformers provide better agreement and none help explain the bands observed at 1145 or 1581 cm⁻¹, see Supporting Information Figure S6. Furthermore, none of the [DKM+H]⁺ structures reproduce the experimental spectrum either, as shown in Supporting Information Figure S7.

Thus, we tentatively identify the [AsnThr+H–NH₃]⁺ species as a mixture of the low-energy [Suc+H]⁺-1.1, 1.2, 1.3, and 1.5 species. An equilibrium distribution of conformers at 298 K suggests that all five of the low-energy [Suc+H]⁺ species could be appreciably populated, although the B3LYP and MP2 levels of theory appear to be capturing the reaction dynamics better, as they predict that [Suc+H]⁺-1.1, 1.2, 1.3, and 1.5 would have populations of 28, 16, 41, and 14% (B3LYP) and 25, 65, 7, and 3% (MP2), respectively. Given the overall modest agreement, we cannot rule out the possibility that other conformers or structures contribute to the spectrum;

however, we have not located any additional low-energy species that reproduce the spectrum better.

Theoretical Results for Sequential Dissociation Channels from the Deamidation Product and IRMPD Spectrum of $[AsnThr+H-NH_3-H_2O]^+$ (m/z 199)

Dissociation of the succinimide deamidation product was experimentally found to exhibit bifurcating pathways leading to the sequential losses of NH₃ (forming m/z 200) and H₂O (forming m/z 199) in the TCID studies. These products have similar intensities at the highest energy shown, where m/z 199 has the lower apparent threshold and dominates at lower energies (Figure 2). Analogous losses were observed in the IRMPD experiments (in a 1:4 ratio). These relative intensities are consistent with the loss of H₂O having the lower threshold, but the comparison indicates different activation conditions in the two techniques, in addition to different contributions to the m/z 199 product from the m/z 216 precursor. The lowest energy pathway located for sequential ammonia loss from the 298 K MP2 [Suc+H]⁺ GS, [Suc+H]⁺-1.2, forms an oxo-vinyl ketone substituted oxazolone via the tight TS_{S-N} lying 355 – 395 kJ/mol above the [AsnThr+H]⁺ GS, Table 1. In contrast, three lower energy pathways were found for the alternative sequential dehydration of $[Suc+H]^+$ forming m/z 199. An overview of these dehydration pathways is given in Figure 5, where it can be seen that paths O1 and O3 lose the hydroxyl group from the carboxylic acid, whereas O2 eliminates the hydroxyl group from the Thr side chain. The lowest energy pathway (as shown in Scheme 1) yields an amino-substituted bicyclic species, [Suc+H-18]+-1, via a pathway predicted to be rate-limited by the tight TS_{S-O1} at the B3LYP (236 kJ/mol) and B3P86 (245 kJ/mol) levels of theory, see Table 1. B3LYP-GD3BJ and MP2(full) instead suggest a product limited pathway with a reaction energy of 244 and 225 kJ/mol, respectively. Two higher energy pathways were also located (again leading to amino-substituted bicyclic structures [Suc+H-18]+ 2 and [Suc+H-18]⁺-3, Figure 5) and are limited by their tight TSs in both cases. TSs-02 and TSs-03 lie 7 – 43 and 31 – 39 kJ/mol, respectively, higher in energy than the rate-limiting energies of path 01.

The IRMPD spectrum of the m/z 200 species could not be taken because the intensity of the precursor ion was too low; however, that for [AsnThr+H-NH₃-H₂O]⁺ at m/z 199 was sufficient for IR interrogation. Interestingly, the IRMPD spectrum (Figure 6) is not reproduced fully on the basis of a single [AsnThr+H-NH₃-H₂O]⁺ isomer. Instead, the major spectral features located at 1855 (cyclic carbonyl CO stretch), 1786 (carboxylic acid CO stretch along with contributions from COH bend), 1576 (cyclic C=N stretch), 1491 (NCO ring bend, amino NH₂ bend, and CH motions), and 1145 cm⁻¹ (ring distortions and carboxylic acid COH bend) in the calculated [Suc+H-18]+-2 spectrum reproduce nearly the entire spectrum well (including relative intensities), except for the small band observed at 1955 cm⁻¹. This band is instead reproduced by either the [Suc+H-18]⁺-1 or [Suc+H-18]+-3 isomers, which have predicted bands at 1976 and 1965 cm⁻¹ (carbonyl CO stretch of the oxazolone ring), respectively. In both cases, composite spectral modeling indicates that contributions from [Suc+H-18]+2 dominate, where an approximate 85%:15% [Suc+H-18]+-2:[Suc+H-18]+1 ratio is found to reproduce the spectrum well across the entire range, see Supporting Information Figure S8. Nearly as good of a match is observed when an 85%:15% [Suc+H-18]+-2:[Suc+H-18]+-3 ratio is used instead. Overall, B3LYP, B3LYP-GD3BJ, and B3P86 levels of theory predict that pathways O1 and O2 should be competitive, with O1 favored by 7 – 14 kJ/mol, whereas O3 is at least 23 kJ/mol higher in energy. In contrast, the MP2 level of theory predicts the O1 pathway is favored by about 40 kJ/mol compared to the O2 and O3 pathways, which have similar energies. Interestingly, m/z 199 formed via the O1 pathway can also be formed via secondary ammonia loss from the dehydration product with competitive energies, as discussed further in the next section.

Theoretical Results for [AsnThr+H]⁺ Dehydration and IRMPD Spectrum of [AsnThr+H–H₂O]⁺ (m/z 216)

Competitive pathways, resulting from dehydration of the carboxylic acid or the threonine side chain, were located for the formation of m/z 216 from [AsnThr+H]⁺. At 0 K, the B3LYP-GD3BJ and MP2 levels of theory suggest the lowest energy pathway for dehydration of [AsnThr+H]⁺ (Figure 7) involves the carboxylic acid and results in the formation of a protonated

oxazolone structure, [OxaO+H]⁺, via a mechanism analogous to that reported in other [AsnXxx+H]⁺ studies [8, 10, 11]. The reaction proceeds through rate-limiting TS_{O-OxaO} (120 – 129 kJ/mol higher in energy than the GS, Table 1), characterized by motions of a proton transfer from CO¹s to O³H, bond rupture of C-O³, and ring formation (CO¹-CO²). All levels of theory predict this reaction is limited by this tight TS, located 13 – 32 kJ/mol above the products.

Additionally, we located competitive pathways that lead to a protonated oxazoline structure, [OxaI+H]⁺ (Figure 7), via dehydration of the Thr side chain. Interestingly, these pathways involve the formation of a tetrahedral intermediate formed via TS_{O-OxaI(tet)}, which is characterized by motions of O^{2s}-C bond formation as well as proton transfer from O^{2s} to O^{1s} and located 101 – 114 kJ/mol higher in energy than the GS. From the tetrahedral intermediate, proton transfer to the protonated O¹ site from either the asparaginyl side-chain, O^{1s} via TS_{O-Oxal-1}, or the N-terminus, N¹ via TS_{O-Oxal-2}, results in the formation and subsequent dissociation of the water leaving group. These two pathways are within 0.7 - 4 kJ/mol of each other, Table 1, such that they should be very competitive. At 0 K, all levels of theory except B3P86 suggest that proton transfer from O^{1s} via rate-limiting TS_{O-OxaI-1} (117 – 129 kJ/mol above the GS) is lowest in energy, whereas 298 K reaction energies at all levels of theory except MP2 predict that proton transfer from N¹ via rate-limiting TS_{O-OxaI-2} is lowest in energy. The B3P86 level indicates that this latter pathway, with rate-limiting TS_{O-OxaI-2} energies 116 – 131 kJ/mol above the GS, is favored (compared to oxazolone formation) at 0 K and 298 K by 13.3 and 20 kJ/mol, respectively. All other levels of theory predict that oxazolone and oxazoline formation should be more competitive, with predicted reaction energies within 6 kJ/mol of each other. Both oxazoline pathways generate the same ground [OxaI+H]⁺ + H₂O structure that lies 47 – 61 kJ/mol above the GS reactants across all levels of theory, 42 - 51 kJ/mol lower in energy than the [OxaO+H]+ + H₂O products. Notably, these dehydration processes are 7-25 kJ/mol lower in energy than the deamidation process via TS_{N-Suc} , a difference qualitatively observed experimentally, see Figure 2.

Sequentially, $[OxaO+H]^+$ can lose ammonia to form m/z 199 (as also formed via the O1 mechanism described above) via a product limited pathway 240 – 264 kJ/mol above the GS, 4 –

21 kJ/mol higher in energy than the O1 pathway. The sequential loss of ammonia to form an isobaric m/z 199 product from $[OxaI+H]^+$ was explored as well. Here, the pathway leading to $[OxaI+H-17]^+$ was found to be the lowest energy pathway with rate-limiting energies of 192-204 kJ/mol above the GS reactants and 32-52 kJ/mol lower in energy than the O1 mechanism. Thus, contributions from all three competitive pathways likely influence the m/z 199 cross section, although the threshold region is likely to be dominated by the $[OxaI+H-17]^+$ pathway. An overview of the TSs leading to m/z 199 from $[OxaO+H]^+$ and $[OxaI+H]^+$ are given in Figure S9.

The experimental [AsnThr+H–H₂O]⁺ IRMPD spectrum is given in Figure 8, along with calculated spectra for the ground structures of [OxaO+H]⁺, [OxaI+H]⁺, and protonated monoketopiperazine ([MKP+H]⁺) isomers. Notably, the latter [MKP+H]⁺ structure is the lowest energy m/z 216 product structure located, although no competitive pathways (compared to energies required for [OxaO+H]⁺ and [OxaI+H]⁺ formation) were located for the production of [MKP+H]⁺. Thus, it is unlikely this structure would be formed experimentally. This observation is consistent with the poor spectral reproduction of the experimental [AsnThr+H–H₂O]⁺ IRMPD features by the [MKP+H]⁺ structure, Figure 8. Similarly poor reproduction is observed for the [OxaO+H]⁺ spectrum. In particular, there is no spectral evidence for the band predicted at 1926 cm⁻¹ (CO stretch of the oxazolone ring), suggesting that oxazolone formation does not occur under these experimental conditions.

Instead, Figure 8 shows that the calculated [OxaI+H]⁺ reproduces most of the experimental features. Specifically, predicted bands centered at 1797 (CO² stretch), 1691 (CO^{1s} stretch and N^{1s}H₂ bend), and 1603 cm⁻¹ (N¹H₂ bend, C=N stretch, and N^{1s}H₂ bend) correspond well with experimental features at 1793, 1697, and 1606 cm⁻¹, respectively. Modest agreement is observed for lower frequency bands. Calculated bands located at 1476 (NH wag and CO stretch of the oxazoline ring), 1390 (CH₃ umbrella and CH₂ wag), and 1148 cm⁻¹ (COH bend) reproduce the frequencies of experimental features (1468, 1392, and 1149 cm⁻¹) well, although obvious intensity discrepancies are observed.

Thus, the $[OxaI+H]^+$ GS is identified as the m/z 216 $[AsnThr+H-H_2O]^+$ species present experimentally. Energetically, the formation of an oxazoline $[OxaI+H]^+$ structure is consistent with energies at the B3LYP and B3P86 levels of theory at both 0 and 298 K, whereas B3LYP-GD3BJ and MP2 levels indicate that oxazolone $[OxaO-H]^+$ formation is favored by 3-6 kJ/mol. This observation suggests that these former levels of theory potentially have a better handle on the reaction dynamics for dehydration of $[AsnThr+H]^+$.

Cross Section Modeling

Equation 1 was used to analyze the thresholds for the primary competitive deamidation and dehydration channels from the decomposition of [AsnThr+H]⁺. Here, both primary channels were modeled simultaneously in order to account directly for competition. Using parameters given in Table 4, the data were reproduced over the full energy and magnitude ranges, as shown in Figure 9. TS frequencies used for the cross section modeling were taken from the theoretical results discussed above.

We first analyzed the data using the tight TS_{N-Suc} and $TS_{O-Oxal-1}$ parameters for deamidation and dehydration, respectively. (These parameters were used first because of the observation of succinimide and oxazoline formation in the IRMPD experiments, despite the energetic favorability of oxazolone formation at several levels of theory.) Our analysis shows that in order to fit the data accurately in the threshold region as well as over the full energy range, the low-frequency modes ($<900~cm^{-1}$) for TS_{N-Suc} need to be loosened by $\sim23\%$ while holding those for $TS_{O-Oxal-1}$ constant. Similar frequency scaling is required to fit the threshold region using TS_{N-Suc} and $TS_{O-Oxal-2}$ parameters. Here, the low-frequency modes of TS_{N-Suc} were loosened by $\sim25\%$ while holding those for the tight $TS_{O-Oxal-2}$ constant. Such scaling results in a good fit through the threshold region, see Figure 9. Compared with using $TS_{O-Oxal-1}$, this approach results in higher thresholds for both deamidation and dehydration, by 0.02 and 0.07~eV, respectively. This appears to be a result of the tighter character of $TS_{O-Oxal-1}$ compared to $TS_{O-Oxal-2}$. Note that a comparable fit can be achieved by instead tightening the low-frequency modes of $TS_{O-Oxal-2}$ (by the same 25%) while holding those for TS_{N-Suc} constant. As shown in Table 4, this leads to a reduction in the threshold energies of

both channels by 0.15 - 0.2 eV, because of differing kinetic shifts. In general, we believe it is more appropriate to scale the frequencies of the less intense channel, a conclusion that can be checked by comparison of the experimental threshold energies with theoretical predictions, see below. Previous thermochemical studies of [AsnGly+H]⁺, [AsnAla+H]⁺, and [AsnVal+H]⁺ also involved scaling of the less intense competitive channel [8, 10, 11].

Given the possibility to also form [Fur+H]⁺ (on the basis of the theoretical energy competition between succinimide and furanone formation), the data were also modeled using molecular parameters for furanone formation. Note that the MP2 and B3LYP-GD3BJ levels of theory do predict a product limited pathway; however, because TS_{N-Fur} lies only 9 and 18 kJ/mol below the product asymptote at these levels, this TS can still limit product formation above energies of the product asymptote. Therefore, these data were fit using parameters for TS_{N-Fur}, consistent with the B3LYP and B3P86 prediction of a tight TS limited pathway. Here, a comparable fit (to that obtained via TS_{N-Suc} modeling) was achieved using parameters also given in Table 4, where this approach required less frequency scaling (only 10%) in order to fit the data in the threshold region. Nearly isoenergetic thresholds (compared to those measured using TS_{N-Suc} parameters) were found via this approach, Table 4. Given the fact that the IRMPD results definitively show formation of the succinimide (Figure 4), the threshold energies obtained and discussed below for deamidation are assigned to this succinimide product. This assignment can be checked by comparison of the experimental energetics with theory, as detailed below.

As shown in Table 4, the data were also modeled competitively with parameters for oxazolone formation via TS_{O-OxaO} and deamidation via TS_{N-Suc} and TS_{N-Fur} . Similar frequency scaling (compared to what was used in the analysis of alternative oxazoline formation) is required for the low-frequency modes of TS_{N-Suc} (loosened by ~25%) in order to reproduce the threshold region. This approach results in deamidation and dehydration thresholds similar to those found using TS_{N-Suc} and $TS_{O-OxaI-1}$ parameters. Modeling using TS_{O-OxaO} and TS_{N-Fur} parameters also results in similar threshold energies. Also shown in Table 4 are $\Delta S^{\dagger}_{1000}$ values, where negative entropies of activation are found for dehydration (-36, -20, and -25 J/K mol for $TS_{O-OxaI-1}$,

TS_{O-Oxal-2}, and TS_{O-OxaO}, respectively) and succinimide formation (-46 J/K mol when the frequencies are unscaled), consistent with the tight character of these pathways.

Conversion of Thermodynamic Parameters from 0 to 298K

For comparison of the thermodynamic information obtained here experimentally to room temperature conditions, Table 5 provides the conversion from 0 K thresholds to 298 K enthalpies and free energies. This conversion is accomplished using the rigid rotor/harmonic oscillator approximations with rotational constants and vibrational frequencies calculated at the B3LYP/6-311+G(d,p) level. Uncertainties listed are determined by scaling the vibrational frequencies by \pm 10%.

Discussion

Experimental versus Theoretical Results

The best agreement between the energetics obtained from experiment and theory comes from the modeling of dehydration and deamidation via $TS_{O-Oxal-2}$ and TS_{N-Suc} parameters. Here, the experimentally determined 0 K threshold for dehydration was found to be 117 ± 5 kJ/mol. The threshold is within experimental uncertainty of the B3P86 value, 116 kJ/mol, Table 6, whereas the remaining three levels of theory predict onsets of 130 - 131 kJ/mol. The alternative model using altered $TS_{O-Oxal-2}$ and frozen TS_{N-Suc} molecular parameters yields an experimental threshold that disagrees with theory by at least 24 ± 7 kJ/mol (Table 4), more than a typical error in such TCID and computational analyses [8, 10, 11, 39-42]. Confirmation that loosening the TS_{N-Suc} parameters yields an appropriate model comes from the threshold for the deamidation process leading to succinimide formation. Here, the experimentally determined 0 K threshold (modeled competitively with $TS_{O-Oxal-2}$) was found to be 142 ± 6 kJ/mol, well within experimental uncertainty of the B3LYP-GD3BJ and B3P86 reaction energies (140 and 141 kJ/mol, respectively), Table 6. The B3LYP level of theory predicts a reaction energy just outside of one standard deviation above the measured value, whereas the MP2 reaction energy (127 kJ/mol) lies 15 kJ/mol *lower* in energy than the measured threshold (although in reasonable agreement with

the 123 ± 5 kJ/mol value obtained by tightening the $TSo_{-Oxal-2}$ frequencies). We can also note that the experimental difference in the two thresholds is 27 ± 3 kJ/mol (21 ± 3 kJ/mol for the alternative model). Theory predicts differences of 20 (B3LYP), 9 (B3LYP-GD3BJ), 25 (B3P86), and 2 (MP2), somewhat below the experimental determinations at all levels except B3P86.

Data for dehydration and deamidation were additionally modeled using $TS_{O\text{-}Oxal\text{-}1}$ ($TS_{O\text{-}OxaO}$) and $TS_{N\text{-}Suc}$ parameters, where similar thresholds of 110 ± 5 and 140 ± 8 (111 ± 5 and 142 ± 7) kJ/mol were measured (Table 4). The competitive modeling here results in a dehydration threshold 7 - 19 kJ/mol lower in energy than predicted reaction energies such that the data appear to be more consistent with $[OxaI+H]^+$ formation via $TS_{O\text{-}Oxal\text{-}2}$ rather than $TS_{O\text{-}Oxal\text{-}1}$ or $TS_{O\text{-}OxaO}$. This is also consistent with theory predicting the former TS is lowest in energy.

As discussed above, the cross section data was also modeled using parameters for furanone formation via TS_{N-Fur} along with dehydration via TS_{O-OxaI-2}. Nearly isoenergetic thresholds (compared to those obtained via the analysis with TS_{N-Suc}) were found for dehydration and deamidation, 117 ± 5 and 141 ± 6 kJ/mol, respectively (Table 4). Thus, similar agreement to theory is observed for the dehydration channel. This deamidation threshold is within or nearly within experimental uncertainty of the B3LYP, B3LYP-GD3BJ, B3P86, and MP2 reaction energies for furanone formation (137, 149, 145, and 143 kJ/mol, respectively). Thus, on the basis of the TCID and theoretical results, either deamidation product is consistent with the experimental threshold energy, whereas the IRMPD spectra clearly indicate that [Suc+H]⁺ is the product formed exclusively, see Figure 4. One possible explanation for these observations relates to the energies of the sequential reactions. The lowest energy decomposition pathway from [Fur+H]⁺ is sequential ammonia loss, which is 76 - 118 kJ/mol higher in energy than the lowest energy pathway for the sequential dehydration of [Suc+H]⁺. Therefore, it is possible that during formation of the [AsnThr+H-NH₃]⁺ product in the ion trap, both [Fur+H]⁺ and [Suc+H]⁺ structures were formed, but the IRMPD response is more sensitive to the [Suc+H]⁺ species. Another contributor to the different observations is the different activation conditions in the two experiments. The fast, singlecollision conditions in TCID allow entropically favored products to be formed facilely once enough energy is available, whereas the slow-heating conditions of SORI preferentially yield only the lower energy products. Thus, the ratio of succinimide:furanone products could be different in both studies, with more furanone formation likely at elevated collision energies in the TCID studies.

The consistent agreement between experiment and theory in Table 6 suggests that the necessary experimental conditions to produce thermal ions were used and confirms that the mechanisms located for these reactions are reasonable pathways. In this case, both succinimide and furanone isomers likely form in the TCID deamidation process throughout the energy range explored, although furanone formation was not confirmed spectroscopically. The need to scale low frequency modes for TS_{N-Suc} (and TS_{N-Fur}), however, indicates that theoretical calculations do not adequately represent how loose/tight the transition states for these competitive pathways are (as also observed in previous studies [8, 10, 11, 40]), consistent with Gaussian warnings that frequencies below ~900 cm⁻¹ are not always reliable [55].

Comparison to Deamidation Studies of [AsnGly+H]+, [AsnAla+H]+, and [AsnVal+H]+

Experimentally, deamidation of [AsnGly+H]⁺, [AsnAla+H]⁺, [AsnVal+H]⁺, and [AsnThr+H]⁺ either leads to succinimide [8] or furanone formation [10], or both [9, 11]. In summary, TCID studies of [AsnGly+H]⁺ [8] suggest that succinimide formation is favored at threshold energies, with contributions from furanone formation at higher energies, although no structural identification of these deamidation products have been confirmed via spectroscopic studies. IRMPD studies of [AsnAla+H]⁺ showed that bifurcating succinimide and furanone deamidation pathways contribute to the deamidation channel [9]. [AsnAla+H]⁺ TCID studies confirmed the competitive nature of these pathways, where furanone formation is favored at threshold energies and contributions from succinimide formation are likely at higher collision energies [11]. For the largest n + 1 residues evaluated in this series of systems (Val and Thr), deamidation exclusively leads to furanone and succinimide formation, respectively, as determined spectroscopically [10], although theory suggests that furanone formation could play a role in the deamidation process of [AsnThr+H]⁺. Thus, increasing the size of the aliphatic n + 1 residue

appears to favor furanone formation, whereas a combination of steric effects and incorporation of different functional groups (i.e., the hydroxyl group of the Thr side chain) favors succinimide formation. Below, we explore a complete evaluation of the energetic, structural, and solvation effects that play a role in the deamidation processes of these four systems.

Energetic Effects. Interestingly, increasing the size of the C-terminal residue side chain has independent effects on the theoretical reaction energetics of succinimide and furanone formation. As shown in Table 6, rate-limiting TSs leading to succinimide formation increase monotonically as the size of the C-terminal residue side chain increases, presumably the result of steric hindrance for the aliphatic side chains, although inductive effects may begin to play a more significant role when functionalized side chains are considered. Specifically, relative to [AsnGly+H]⁺, rate-limiting TSs for the AsnAla and AsnVal species exhibit increases in energy of ~12 and ~21 kJ/mol at the B3LYP, B3LYP-GD3BJ, and B3P86 levels, and 4 and 12 kJ/mol at the MP2(full) level, respectively. In contrast, no obvious energetic trend is observed for furanone formation. At the B3LYP and B3P86 levels, TS energies are identical for the Gly, Ala, and Val side chains. Reaction energies at the B3LYP-GD3BJ level are similar and decrease slightly as the size of the aliphatic side chain increases. MP2 exhibits a larger energetic spread, but this is primarily because only this level predicts a product limited pathway.

A direct comparison of 0 K [AsnThr+H]⁺ relative energies to the three aliphatic dipeptides is misleading because the [AsnThr+H]⁺ system exhibits a different GS conformation compared to those in the aliphatic systems. Specifically, [AsnThr+H]⁺ [N¹,CO¹s,CO¹]-ttgtgtt and gggtgtt conformers are stabilized by a hydrogen bond involving the side-chain hydroxyl group. Thus, the ttgtttt conformer, which is 14 – 23 kJ/mol higher in energy than the ttgtgtt or gggtgtt GSs, is analogous to the GSs located for the aliphatic systems. Accounting for this difference (as shown by the bracketed values in Table 6), the energy of both rate-limiting [AsnThr+H]⁺ deamidation TSs decrease such that for both Suc and Fur formation, deamidation from [AsnThr+H]⁺ is favored over deamidation from [AsnVal+H]⁺ (by averages of 39 and 12 kJ/mol, respectively). This is then consistent with accelerated deamidation rates observed in condensed phase studies of AsnThr

sequences (when Thr is the n + 1 residue, deamidation rates are ~ 5 times faster than when Val is present) [1].

Mean absolute deviations (MADs) between experimental and theoretical thermochemistry were calculated collectively for the deamidation and dehydration processes of [AsnGly+H]⁺, [AsnAla+H]⁺, [AsnVal+H]⁺, and [AsnThr+H]⁺. Note that for the [AsnAla+H]⁺ and [AsnVal+H]⁺ systems, furanone formation was favored at threshold energies, such that reaction energies for furanone formation are used for comparison. Overall MADs (Table 6, for the observed channels denoted non-bracketed values) for deamidation and dehydration were calculated to be 11 ± 7 , 10 ± 8 , 10 ± 7 , and 9 ± 4 kJ/mol at the B3LYP, B3LYP-GD3BJ, B3P86, and MP2 levels of theory, respectively. Overall, there is reasonable agreement at all levels of theory.

Structural Effects. One means to understand how the neighboring n+1 residues influence deamidation rates is to examine the Mulliken partial charges, δ , induced at the rate-limiting steps. A comparison of structural (steric) and inductive effects of rate-limiting TSs in [AsnThr+H]⁺ and [AsnVal+H]⁺ (the two systems to exclusively yield one deamidation product in the IRMPD studies) for the lowest energy furanone and succinimide formation pathways is given in Figure S10. All rate-limiting TSs are characterized by similar vibrational motions, such that differences in partial charges of the major atoms involved in the TS should be a result of a combination of structural and inductive effects. Magnitudes of inductive effects decrease with an increase in the distance between the groups initiating the polarization and the atom on which δ is being inspected. Thus, for the succinimide pathway, the close proximity of the Thr side-chain OH to the NH₃ leaving group leads to larger δ values and can help stabilize the partial negative charge on the carbonyl carbon. This could have a favorable effect on reaction energetics. On the other hand, the side chain is not directly facilitating the furanone reaction, such that the inductive effects here are probably minimized, indicated by the smaller absolute δ values. Another way to quantify this phenomenon is to examine the differences in partial charges, $\Delta \delta = \delta_A - \delta_B$, between atoms A and B: 0.10 and 0.23 for [Fur+H]⁺ formation versus 0.69 and 0.51 for [Suc+H]⁺ from [AsnThr+H]⁺ and [AsnVal+H]⁺, respectively. The larger differences observed for [Suc+H]⁺ formation indicate

that inductive effects from the OH group have a more significant effect on the reaction dynamics for this pathway, compared to the steric effects in [Fur+H]⁺ formation. Additionally, from a structural perspective, the Thr side chain would likely still have the ability to orient itself into a favorable hydrogen bonding environment in a larger, more biologically relevant system.

Solvation Effects. From an experimental point of view, our results suggest that steric effects alone (a key aspect of previous n + 1 residue studies) [1] may not be the dominant factor in controlling the rate of deamidation under our experimental conditions. In particular, nearly isoenergetic thresholds were determined for the [AsnGly+H]⁺, [AsnAla+H]⁺, and [AsnVal+H]⁺ systems [8, 10, 11], although condensed phase studies suggest that the rate of deamidation in the latter two systems are on the order of 20 and 200 times slower than that of -Asn-Gly- sequences [1]. (Notably, the deamidation process of [AsnThr+H]⁺ was measurably higher in energy than from $[AsnGly+H]^+$ by 14 ± 9 kJ/mol.) Thus, it appears that the accessibility to water may be an important factor regarding the deamidation process, a conclusion that has been previously drawn from theoretical studies [16]. Clearly, understanding the relationship between gas and condensedphase pathways is important, and we have previously reported on the effects of solvation on mechanisms analogous to those located here for succinimide and furanone formation, in addition to one additional mechanism for succinimide formation via a tetrahedral intermediate [7]. The only process accelerated via water solvation is succinimide formation via the tetrahedral intermediate, suggesting this may be the dominant pathway in vivo. The proton transfers involved in the ratelimiting step are facilitated by the addition of solvent such that water mediation effects are clearly noticeable. On the other hand, the deamidation mechanisms (specifically the rate-limiting TSs) presented here (Figure 3) are characterized by bond ruptures and formation, where the only role of the water group is stabilization of the NH₃⁺ group. Thus, although asparaginyl systems can deamidate via low energy pathways leading to alternative cyclic structures in the gas phase, furanone formation is not observed in solution and succinimide formation (potentially via the tetrahedral intermediate) is most commonly reported [7, 12, 16].

One additional consideration here is the introduction of different side-chain chemistry via the threonine hydroxyl group. Presumably, this hydroxyl group can facilitate the proton transfers required for succinimide formation via the tetrahedral intermediate such that the likely TSs along pathways leading from the tetrahedral intermediate were explored. Here, the effects of water solvation on these pathways was considered both implicitly as well as explicitly via the addition of one water molecule. Geometry optimizations of these mono-solvated reaction species were done at the B3LYP/6-311+G(d,p) level of theory, and single point energies were calculated at the B3LYP, B3P86, and MP2/6-311+G(2d,2p) levels of theory. Both geometry optimizations and single point energies included use of self-consistent reaction field theory via the polarizable continuum model [58, 59].

The first pathway located follows a mechanism analogous to that proposed previously for [AsnGly+H]⁺ [8]. From the likely tetrahedral intermediate formed, the water molecule facilitates a proton transfer from the hydroxyl group (of the tetrahedral center in the succinimide ring) to the adjacent NH₂ amino group via rate-limiting TS_{Tet-1-H2O}, Figure S11. This results in the loss of NH₃ and the formation of a protonated succinimide structure, where protonation now occurs at site 4 as shown in Scheme 2 rather than at the N¹ site 1. This series of proton transfers requires 128 – 188 kJ/mol. An additional TS (TS_{Tet-2-H2O}, Figure 10) was located, where both the water molecule and the Thr side-chain hydroxyl group stabilize the proton transfers required for NH₃ formation. Involvement of the side chain results in a lower energy TS by 22 – 24 kJ/mol. This pathway leads to the same protonated succinimide structure detailed above, [Suc+H]⁺-4.1.

Comparatively, the rate-limiting TS (TS_{N-Suc-H2O}) of the solvated pathway paralleling the gas-phase mechanism leading to [Suc+H]⁺-1.2 formation lies 154 – 185 kJ/mol above the GS, 18 – 48 kJ/mol higher in energy than the rate-limiting TS_{Tet-2-H2O}. Here, the rate-limiting TS adopts a conformation where the water molecule stabilizes the charge at site 2 of the Suc ring (Scheme 2). Interestingly, we also tried to locate a TS characterized by the analogous conformation as TS_{N-Suc} with the water molecule interacting with the NH₃ leaving group. In this case, the added water

molecule inhibited dissociation of the NH₃ group. Thus, we explored alternate water–molecule interaction sites, leading to the location of TS_{N-Suc-H2O}.

These solvated energetic results indicate that for –Asn–Thr– sequences, succinimide formation via the tetrahedral intermediate and TS_{Tet-2-H2O} is energetically favored and could be observed under solvated physiological conditions. However, TS_{Tet-2-H2O} is 17 kJ/mol above TS_{N-Suc} at the B3LYP level of theory such that if deamidation was occurring in a region of a protein with limited access to water (e.g., inside of a tightly packed region or within a hydrophobic core), the reaction may proceed via the pathway presented in Figure 3. Therefore, the extension of these deamidation studies to systems characterized by different conformational constraints and varying degrees of likely water accessibility would be valuable.

Conclusions

The decomposition of [AsnThr+H]⁺ was studied by measuring kinetic energy dependent thresholds for collision-induced dissociation with Xe using a GIBMS, where major reaction product species were further evaluated using IRMPD action spectroscopy. This combination of techniques allows for the unambiguous structural identification of key [AsnThr+H–NH₃]⁺, [AsnThr+H–H₂O]⁺, and [AsnThr+H–NH₃–H₂O]⁺ species as well as the energetic analysis of the associated reaction mechanisms.

Deamidation of [AsnThr+H] $^+$ yielded a succinimide product, as confirmed via our spectroscopic analyses. Theoretical results indicate that both succinimide and furanone formation could contribute to the deamidation process as they are energetically comparable with Suc lower by 4-16 kJ/mol at three levels of theory and Fur lower by 13 kJ/mol at the B3LYP level. Analysis of TCID thresholds for deamidation using molecular parameters for each of these pathways yielded isoenergetic values, 142 ± 6 kJ/mol and 141 ± 6 kJ/mol, respectively (Table 4), which are within experimental uncertainty of predicted reaction values at several levels of theory. Thus, the TCID analysis may be consistent with both succinimide and furanone formation, with identification of the succinimide deamidation product being confirmed by IRMPD analyses. Decomposition of

[AsnThr+H]⁺ also resulted in dehydration of the complex, where a threshold energy of 117 ± 5 kJ/mol was measured using parameters for protonated oxazoline formation, 25 ± 1 kJ/mol lower in energy than deamidation. IRMPD analyses confirmed the exclusive formation of a protonated oxazoline structure (resulting from dehydration of the side chain, rather than the backbone), which we found to be energetically competitive with oxazolone formation on a theoretical basis.

Bifurcating pathways were observed for the sequential losses of NH₃ and H₂O from the [AsnThr+H–NH₃]⁺ product ion. Here, the IRMPD analysis confirmed the presence of multiple [AsnThr+H–NH₃–H₂O]⁺ bicyclic species contributing to the spectrum. Composite modeling indicated that an 85%:15% [Suc+H–18]⁺-2:[Suc+H–18]⁺-1 or [Suc+H–18]⁺-2:[Suc+H–18]⁺-3 ratio reproduces the spectrum well across the entire spectral range, although the identified reaction mechanism leading to [Suc+H–18]⁺-2 is 7 – 43 kJ/mol higher in energy than the analogous pathway leading to [Suc+H–18]⁺-1. The pathway located for [Suc+H–18]⁺-3 may also be competitive with these lower energy pathways, and is located 31 – 39 kJ/mol higher in energy than the pathway leading to [Suc+H–18]⁺-1. These energetics suggest that [Suc+H–18]⁺–2 and 1 are the most likely products.

Regarding the comparison to our previously studied [AsnGly+H]⁺, [AsnAla+H]⁺, and [AsnVal+H]⁺ systems, our comprehensive results suggest that for aliphatic n + 1 residues, steric effects play a dominant role in controlling the rate of deamidation. However, for n + 1 residues possessing functional groups (e.g., hydroxyl groups), side-chain functionality is a contributing factor in controlling the deamidation reaction. Notably, additional factors such as access to water solvent may play important roles in the condensed-phase deamidation of Asn residues. Clearly, additional studies involving other n + 1 residues will aid in the understanding of the specific interactions that either hinder or accelerate the deamidation process. Such experiments are currently being conducted in our laboratories.

Acknowledgements. The IRMPD spectrum of [AsnThr+H–H₂O]⁺ was recorded by Thijs P. J. Geurts, MSc, and is part of a forthcoming study presenting a more extensive set of dehydrated

dipeptides. We gratefully acknowledge the FELIX staff for technical support and the *Nederlandse Organisatie voor Wetenschappelijk Onderzoek* (NWO) for financial support of the FELIX Laboratory. Financial support for this project was provided by NWO Chemical Sciences under VICI grant 724.011.002 and by the National Science Foundation, Grant No. CHE-1664618. Computing resources were generously provided by NWO Physical Sciences (EW) and the SurfSARA Supercomputer Center under grant 17603 and by the Center for High Performance Computing (CHPC) at the University of Utah.

Supporting Information. Figures S1 – 11 show major species along the reaction coordinate leading to **[Suc+H]**⁺-**4.1** and [AsnThr+H–H₂O–NH₃]⁺, select [Suc+H]⁺, [Fur+H]⁺, and [DKM+H]⁺ conformers, Mulliken charges for TSs leading to [Suc+H]⁺ and [Fur+H]⁺ formation from [AsnThr+H]⁺ and [AsnVal+H]⁺, and spectral comparisons between experiment and theory for [DKM+H]⁺ and composite modeling of **[Suc+H–18]**⁺ structures.

AUTHOR INFORMATION

Corresponding Authors

*E-mail: j.oomens@science.ru.nl (J.O.).

*E-mail: armentrout@chem.utah.edu (P.B.A.).

ORCID

J. Martens: 0000-0001-9537-4117 G. Berden: 0000-0003-1500-922X J. Oomens: 0000-0002-2717-1278

P. B. Armentrout: 0000-0003-2953-6039

Notes

The authors declare no competing financial interest.

References

- [1] N.E. Robinson, A.B. Robinson, Molecular Clocks, Proc. Natl. Acad. Sci., 98 (2001) 944–949.
- [2] M.R. Nilsson, M. Driscoll, D.P. Raleigh, Low Levels of Asparagine Deamidation Can Have a Dramatic Effect on Aggregation of Amyloidogenic Peptides: Implications for the Study of Amyloid Formation, Protein Sci., 11 (2002) 342-349.
- [3] N.E. Robinson, A.B. Robinson, Molecular Clocks: Deamidation of Asparaginyl and Glutaminyl Residues in Peptides and Proteins, Althouse Press, Cave Junction, OR, 2004.

- [4] J.B. Catterall, M.F. Hsueh, T.V. Stabler, C.R. McCudden, M. Bolognesi, R. Zura, J.M. Jordan, J.B. Renner, S. Feng, V.B. Kraus, Protein Modification by Deamidation Indicates Variations in Joint Extracellular Matrix Turnover, J. Biol. Chem., 287 (2012) 4640-4651.
- [5] R.C. Stephenson, S. Clarke, Succinimde Formation from Aspartyl and Asparaginyl Peptides as a Model for the Spontaneous Degradation of Proteins, J. Biol. Chem, 264 (1989) 6164-6170.
- [6] R. Tyler-Cross, V. Schirch, Effects of Amino Acid Sequence, Buffers, and Ionic Strength on the Rate and Mechanism of Deamidation of Asparagine Residues in Small Peptides, J. Biol. Chem., 266 (1991) 22549-22556.
- [7] S. Capasso, L. Mazzarella, F. Sica, A. Zagari, S. Salvadori, Kinetics and Mechanism of Succinimide Ring Formation in the Deamidation Process of Asparagine Residues, J. Chem. Soc. Perkin Trans. 2, (1993) 679-682.
- [8] G.C. Boles, R.R. Wu, M.T. Rodgers, P.B. Armentrout, Thermodynamics and Mechanisms of Protonated Asparaginyl-Glycine Decomposition, J. Phys. Chem. B, 120 (2016) 6525-6545.
- [9] L.J.M. Kempkes, J.K. Martens, J. Grzetic, G. Berden, J. Oomens, Deamidation Reactions of Asparagine- and Glutamine-Containing Dipeptides Investigated by Ion Spectroscopy, J. Am. Soc. Mass Spectrom., 27 (2016) 1855-1869.
- [10] L.J.M. Kempkes, G.C. Boles, J. Martens, G. Berden, P.B. Armentrout, J. Oomens, Deamidation of Protonated Asparagine-Valine Investigated by a Combined Spectroscopic, Guided Ion Beam, and Theoretical Study, *J. Phys. Chem. A*, 122 (2018) 2424-2436.
- [11] G.C. Boles, R.R. Wu, M.T. Rodgers, P.B. Armentrout, Protonated Asparaginyl-Alanine Decomposition: A TCID, SORI-CID, and Computational Analysis, J. Am. Soc. Mass Spectrom., 29 (2018) 2341-2359.
- [12] F.A. Konuklar, V. Aviyente, T.Z. Sen, I. Bahar, Modeling the Deamidation of Asparagine Residues Via Succinimde Intermediates, J. Mol. Model., 7 (2001) 147-160.
- [13] N.E. Robinson, A.B. Robinson, Prediction of Primary Structure Deamidation Rates of Asparaginyl and Glutaminyl Peptides Through Steric and Catalytic Effects, J. Pept. Res., 63 (2004) 437-448.
- [14] B. Peters, B.L. Trout, Asparagine Deamidation: pH-Dependent Mechanism from Density Functional Theory, Biochem., 45 (2006) 5384-5392.
- [15] S. Catak, G. Monard, V. Aviyente, M.F. Ruiz-Lopez, Deamidation of Asparagine Residues: Direct Hydrolysis versus Succinimide-Mediated Deamidation Mechanisms, J. Phys. Chem. A, 113 (2009) 1111-1120.
- [16] S. Catak, G. Monard, V. Aviyente, M.F. Ruiz-Lopez, Reaction Mechanism of Deamidation of Asparaginyl Residues in Peptides: Effect of Solvent Molecules, J. Phys. Chem. A, 110 (2006) 8354-8365.
- [17] K. Patel, R.T. Borchardt, Chemical Pathways of Peptide Degradation. III. Effect of Primary Sequence on the Pathways of Deamidation of Asparaginyl Residues in Hexapeptides, Pharm. Res., 7 (1990) 787-793.
- [18] M. Xie, R.L. Schowen, Secondary Structure and Protein Deamidation J. Pharma. Sci., 88 (1998) 8-13.
- [19] A.A. Kossiakoff, Tertiary Structure is a Principal Determinant to Protein Deamidation, Science, 240 (1988) 191-194.
- [20] N.E. Robinson, A.B. Robinson, Prediction of protein deamidation rates from primary and three-dimensional structure, Proc. Natl. Acad. Sci., 98 (2001) 4367-4372.
- [21] B. Lucas, G. Gregoire, J. Lemaire, P. Maitre, J. Ortega, A. Rupenyan, B. Reimann, J.P. Schermann, C. Desfrancois, Investigation of the Protonation Site in the Dialanine Peptide by

- Infrared Multiphoton Dissociation Spectroscopy, Phys. Chem. Chem. Phys., 6 (2004) 2659-2663.
- [22] N.C. Polfer, J. Oomens, Reaction Products in Mass Spectroscopy Elucidated with Infrared Spectroscopy, Phys. Chem. Chem. Phys., 9 (2007) 3804-3817.
- [23] N.C. Polfer, J. Oomens, S. Suhai, B. Paizs, Infrared Spectroscopy and Theoretical Studies on Gas-Phase Protonated Leu-enkephalin and its fragments: direct experimental evidence for the mobile proton, J. Am. Chem. Soc., 129 (2007) 5887-5897.
- [24] C.F. Correia, P.O. Balaj, D. Scuderi, P. Maitre, G. Ohanessian, Vibrational Signatures of Protonated, Phosphorylated Amino Acids in the Gas Phase, J. Am. Chem. Soc., 130 (2008) 3359-3370.
- [25] B.J. Bythell, U. Erlekam, B. Paizs, P. Maitre, Infrared Spectroscopy of Fragments from Doubly Protonated Tryptic Peptides, Chem. Phys. Chem., 10 (2009) 883-885.
- [26] Y.M.E. Fung, T. Besson, J. Lemaire, P. Maitre, R.A. Zubarev, Room-temperature Infrared spectroscopy combined with mass spectrometry distinguishes gas-phase protein isomers, Angew. Chem., 48 (2009) 8340-8342.
- [27] J. Oomens, J.D. Steill, B. Redlich, Gas-Phase IR spectroscopy of Deprotonated Amino Acids, J. Am. Chem. Soc., 131 (2009) 4310-4319.
- [28] A.L. Patrick, C.N. Stedwell, B. Schindler, I. Compagon, G. Berden, J. Oomens, N.C. Polfer, Insights into the Fragmentation Pathways of Gas-Phase Protonated Sulfoserine, J. Mass Spectrom., 379 (2015) 26-32.
- [29] L.J.M. Kempkes, J.K. Martens, J. Grzetic, G. Berden, J. Oomens, Deamidation Reactions of Protonated Asparagine and Glutamine Investigated by Ion Spectroscopy, Rapid Commun. Mass Spectrom., 30 (2016) 483-491.
- [30] G.C. Boles, C.J. Owen, G. Berden, J. Oomens, P.B. Armentrout, Experimental and Theoretical Investigations of Infrared Multiple Photon Dissociation Spectra of Glutamic Acid Complexes of Zn²⁺ and Cd²⁺, Phys. Chem. Chem. Phys., 19 (2017) 12394-12406.
- [31] D. Oepts, A.F.G. van der Meer, P.W. van Amersfoort, The Free-Electron-Laser User Facility FELIX, Infrared Phys. Technol., 36 (1995) 297-308.
- [32] J. Martens, G. Berden, C.R. Gebhardt, J. Oomens, Infrared Ion Spectroscopy in a Modified Quadrupole Ion Trap Mass Spectrometer at the FELIX Free Electron Laser Laboratory, Rev. of Scient. Instrum., 87 (2016) 103108.
- [33] J. Oomens, B.G. Sartakov, G. Meijer, G. von Helden, Gas-Phase Infrared Multiple Photon Dissociation Spectroscopy of Mass-Selected Molecular Ions, Int. J. Mass Spectrom., 254 (2006) 1-19.
- [34] K.M. Ervin, P.B. Armentrout, Translational Energy Dependence of $Ar^+ + XY \rightarrow ArX^+ + Y$ (XY = H₂, D₂, HD) from Thermal to 30 eV c.m., J. Chem. Phys., 83 (1985) 166-189.
- [35] F. Muntean, P.B. Armentrout, Guided Ion Beam Study of Collision-Induced Dissociation Dynamics: Integral and Differental Cross Sections, J. Chem. Phys., 115 (2001) 1213-1228.
- [36] P.B. Armentrout, Not Just a Structural Tool: The Use of Guided Ion Beam Tandem Mass Spectrometry to Determine Thermochemistry, J. Am. Soc. Mass Spectrom., 13 (2002) 419-434.
- [37] R.M. Moision, P.B. Armentrout, An Electrospray Source for Thermochemical Investigation with the Guided Ion Beam Mass Spectrometer, J. Am. Soc. Mass Spectrom., 18 (2007) 1124-1134.
- [38] T. Kim, A.V. Tolmachev, R. Harkewicz, D.C. Prior, G. Anderson, H.R. Udseth, R.D. Smith, Design and Implementation of a New Electrodynamic Ion Funnel, Anal. Chem, 72 (2000) 2247-2255.

- [39] A.L. Heaton, P.B. Armentrout, Thermodynamics and Mechanism of the Deamidation of Sodium-Bound Asparagine, J. Am. Chem. Soc., 130 (2008) 10227-10232.
- [40] A.L. Heaton, P.B. Armentrout, Thermodynamics and Mechanism of Protonated Asparagine Decomposition, J. Am. Soc. Mass Spectrom., 20 (2009) 852-866.
- [41] S.J. Ye, P.B. Armentrout, Absolute Thermodynamic Measurements of Alkali Metal Cation Interactions with a Simple Dipeptide and Tripeptide, J. Phys. Chem. A, 112 (2008) 3587-3596.
- [42] J.E. Carpenter, C.P. McNary, A. Furin, A.F. Sweeney, P.B. Armentrout, How Hot are Your Ions Really? A Threshold Collision-Induced Dissociation Study of Substituted Benzylpyridium "Thermometer" Ions, J. Am. Soc. Mass Spectrom., 28 (2017) 1876-1888.
- [43] E. Teloy, D. Gerlich, Integral Cross Sections for Ion-Molecule Reactions. 1. The Guided Beam Technique, Chem. Phys., 4 (1974) 417-427.
- [44] D. Gerlich, Inhomogeneous rf Fields: A Versatile Tool for the Study of Processes with Slow Ions, Adv. Chem. Phys., 82 (1992) 1-176.
- [45] N. Aristov, P.B. Armentrout, Collision-Induced Dissociation of Vanadium Monoxide Ion, J. Phys. Chem., 90 (1986) 5135-5140.
- [46] N.F. Dalleska, K. Honma, L.S. Sunderlin, P.B. Armentrout, Solvation of Transition Metal Ions by Water. Sequential Binding Energies of $M^+(H_2O)_x$ (x = 1 4) for M = Ti Cu Determined by Collision-Induced Dissociation, J. Am. Chem. Soc., 116 (1994) 3519-3528.
- [47] N.R. Daly, Scintillation Type Mass Spectrometer Ion Detector, Rev. Sci. Instrum., 31 (1960) 264-267.
- [48] T.S. Beyer, D.F. Swinehart, Number of Multiply-Restricted Partitions, Commun. ACM, 16 (1973) 379.
- [49] S.E. Stein, B.S. Rabinovich, On the Use of Exact State Counting Methods in RRKM Rate Calculations, Chem. Phys. Lett., 49 (1977) 183-188.
- [50] S.E. Stein, B.S. Rabinovitch, Accurate Evaluation of Internal Energy Level Sums and Densities Including Anharmonic Oscillators and Hindered Rotors, J. Chem. Phys., 58 (1973) 2438-2445.
- [51] R.G. Gilbert, S.C. Smith, Theory of Unimolecular and Recombination Reactions, Blackwell Scientific, London, 1990.
- [52] P.J. Robinson, K.A. Holbrook, Unimolecular Reactions, Wiley Interscience, New York, 1972.
- [53] M.T. Rodgers, P.B. Armentrout, Statistical Modeling of Competitive Threshold Collision-Induced Dissociation, J. Chem. Phys., 109 (1998) 1787-1800.
- [54] M.T. Rodgers, K.M. Ervin, P.B. Armentrout, Statistical Modeling of Collision-Induced Dissociation Thresholds, J. Chem. Phys., 106 (1997) 4499-4508.
- [55] M.J. Frisch, G.W. Trucks, H.B. Schlegel, G.E. Scuseria, M.A. Robb, J.R. Cheeseman, G. Scalmani, V. Barone, B. Mennucci, G.A. Petersson, H. Nakatsuji, M. Caricato, X. Li, H.P.
- Hratchian, A.F. Izmaylov, J. Bloino, G. Zheng, J.L. Sonnenberg, M. Hada, M. Ehara, K. Toyota, R. Fukuda, J. Hasegawa, M. Ishida, T. Nakajima, Y. Honda, O. Kitao, H. Nakai, T. Vreven, J.A.
- Montgomery, J.E. Peralta, F. Ogliaro, M. Bearpark, J.J. Heyd, E. Brothers, K.N. Kudin, V.N.
- Staroverov, R. Kobayashi, J. Normand, K. Raghavachari, A. Rendell, J.C. Burant, J.M. Millam,
- S.S. Iyengar, J. Tomasi, M. Cossi, N. Rega, J.M. Millam, M. Klene, J.E. Knox, J.B. Cross, V.
- Bakken, C. Adamo, J. Jaramillo, R. Gomperts, R.E. Stratmann, O. Yazyev, A.J. Austin, R.
- Cammi, C. Pomelli, J.W. Ochterski, R.L. Martin, K. Morokuma, V.G. Zakrzewski, G.A. Voth, P. Salvador, J.J. Dannenberg, S. Dapprich, A.D. Daniels, O. Farkas, J.B. Foresman, J.V. Ortiz, J.
- Cioslowski, D.J. Fox, Gaussian 09, Revision A.02, in, Gaussian Inc., Pittsburgh, PA, 2009.

- [56] S. Grimme, S. Ehrlich, L. Goerigk, Effect of the Damping Function in Dispersion Corrected Density Functional Theory, J. Comput. Chem., 32 (2011) 1456-1465.
- [57] M.K. Kesharwani, B. Brauer, J.M.L. Martin, Frequency and Zero-Point Vibrational Energy Scale Factors for Double-Hybrid Density Functionals (and Other Selected Methods): Can Anharmonic Force Fields Be Avoided?, J. Phys. Chem. A, 119 (2015) 1701-1714.
- [58] O. Tapia, O. Goscinski, Self-Consistent Reaction Field Theory of Solvent Effects, Mol. Phys., 29 (1975) 1653-1661.
- [59] M. Cossi, G. Scalmani, N. Rega, V. Barone, New Developments in the Polarizable Continuum Model for Quantum Mechanical and Classical Calculations on Molecules in Solution. J. Chem. Phys., 117 (2002) 43-54.

Table 1. Relative Enthalpies (0 K) and Gibbs Energies (298 K) in kJ/mol of Rate-Limiting Transition States and Products for Major Decomposition Reactions of [AsnThr+H]^{+ a}

Species	B3LYP	B3LYP-GD3BJ ^b	B3P86	MP2(full)
	Dehyo	dration (<i>m/z</i> 216)		
TSo-oxao	128.7 (135.3)	125.4 (128.1)	129.2 (135.8)	120.2 (123.6)
$[OxaO+H]^+ + H_2O$	96.6 (58.0)	112.2 (72.7)	103.6 (61.8)	100.7 (62.6)
TS _{O-OxaI-1}	128.6 (134.7)	128.1 (133.7)	116.6 (119.5)	126.0(129.0)
TSO-OxaI-2	129.7 (132.7)	131.0 (132.3)	115.9 (115.8)	129.8 (129.7)
$[OxaI+H]^+ + H_2O$	46.8 (7.0)	61.6 (20.1)	54.0 (13.5)	58.4 (15.4)
Deamidation (m/z 217)				
TS _{N-Suc}	150.0 (159.9)	140.1 (147.4)	141.0 (150.9)	127.4 (134.1)
$[Suc+H]^+-1.2 + NH_3$	119.9 (83.3)	123.8 (87.8)	124.4 (87.1)	104.5 (64.7)
$TS_{N ext{-}Fur}$	137.2 (138.6)	131.1 (139.2)	144.7 (145.5)	134.2 (132.6)
$[Fur+H]^+-3.1 + NH_3$	127.2 (85.5)	148.6 (107.2)	138.7 (96.3)	143.2 (98.3)
Sequential Ammonia Loss from [OxaI+H] ⁺ (m/z 199)				
TS_{SO-N}	191.9 (151.1)	204.1 (164.5)	193.4 (155.1)	192.8 (152.0)
$[OxaI+H-17]^+ + NH_3$	164.9 (82.3)	193.2 (112.5)	177.9 (95.3)	184.0 (98.2)
Sequential Dehydration from [Suc+H] ⁺ -1.2 (<i>m/z</i> 199)				
TSs-01	236.0 (201.4)	238.2 (204.0)	245.4 (210.1)	209.5 (171.8)
$[Suc+H-18]^+-1 + H_2O$	217.4 (134.9)	243.9 (161.9)	231.5 (148.4)	224.7 (139.2)
TS_{S-O2}	243.1 (203.0)	252.1 (212.3)	258.9 (218.2)	267.8 (224.6)
$[Suc+H-18]^+-2 + H_2O$	167.5 (86.4)	194.0 (114.8)	180.5 (98.8)	183.8 (99.5)
TSs-03	266.6 (226.4)	277.4 (237.4)	283.7 (242.9)	263.7 (220.3)
$[Suc+H-18]^+-3 + H_2O$	236.1 (154.6)	264.1 (184.2)	250.1 (168.0)	250.2 (165.5)
Sequential Ammonia Loss from [Suc+H] ⁺ -1.2 (m/z 200)				
TS _{S-N}	354.8 (304.7)	368.7 (316.9)	394.8 (344.1)	369.1 (315.9)
$[Suc+H-17]^+ + NH_3$	303.7 (217.3)	332.0 (246.7)	337.6 (250.6)	345.5 (255.9)

^a Calculations performed at the stated level of theory using a 6-311+G(2d,2p) basis set with B3LYP/6-311+G(d,p) geometries. Values are given relative to the predicted GS. Gibbs energies in parentheses. Bold indicates the rate-limiting step (TS or product). ^b Calculations performed at the B3LYP-GD3BJ/6-311+G(2d,2p)//B3LYP-GD3BJ/6-311+G(d,p) level.

Table 2. Relative Enthalpies (0 K) and Gibbs Energies (298 K) in kJ/mol for Possible [AsnThr+H–NH₃]⁺ Product Structures^a

	[Suc+H] ⁺		[Fur+H] ⁺		[DKM+H] ⁺	
Protonation	B3LYP	MP2	B3LYP	MP2	B3LYP	MP2
Site						
1	38 (42)	0 (0)	127 (126)	105 (101)	82 (82)	75 (71)
2	72 (73)	47 (44)	b		54 (53)	53 (48)
3	168 (167)	129 (125)	49 (45)	39 (31)	0 (0)	6 (2)
4	30 (30)	6 (2)	134 (131)	123 (116)	86 (84)	69 (64)
5	148 (146)	129 (123)			97 (98)	97 (94)

^a Calculations performed at the stated level of theory using a 6-311+G(2d,2p) basis set with geometries calculated at B3LYP/6-311+G(d,p) level for protonation sites illustrated in Scheme 2. Gibbs energies in parentheses. ^b Protonation at site 2, Scheme 2, leads to opening of the furanone ring.

Table 3. Relative Enthalpies (0 K) and Gibbs Energies (298 K) in kJ/mol of Possible Succinimide and Furanone Deamidation Products of [AsnThr+H]^{+ a}

Species	B3LYP	B3LYP-GD3BJ ^b	B3P86	MP2(full)
10 . 10 4 4	0.0 (1.9)	0.0 (0.0)	0.0 (0.0)	0.0 (2.4)
[Suc+H] ⁺ -1.1	115.9 (81.9)	118.5 (85.0)	118.3 (83.6)	104.2 (67.1)
IC 100+12	4.0 (3.3)	5.3 (2.8)	6.1 (3.5)	0.3 (0.0)
[Suc+H] ⁺ -1.2	119.9 (83.3)	123.8 (87.8)	124.4 (87.1)	104.5 (64.7)
IC 170+12	4.9 (0.0)	13.9 (6.3)	9.0 (2.2)	10.0 (5.5)
[Suc+H] ⁺ -1.3	120.8 (80.0)	132.4 (91.3)	127.3 (85.8)	114.2 (70.2)
ICmal IIII+ 1 4	6.6 (6.6)	8.6 (6.5)	7.8 (6.0)	7.4 (7.8)
[Suc+H] ⁺ -1.4	122.5 (86.6)	127.1 (91.5)	126.1 (89.6)	111.6 (72.5)
[Cual III]† 1 5	9.2 (3.7)		13.7 (6.4)	13.0 (8.0)
[Suc+H] ⁺ -1.5	125.1 (83.7)	С	132.0 (90.0)	117.2 (72.7)
T	11.3 (5.5)	30.1 (22.2)	20.4 (12.7)	39.0 (33.6)
[Fur+H] ⁺ -3.1	127.2 (85.5)	148.6 (107.2)	138.7 (96.3)	143.2 (98.3)
IE1 HII+ 2.2	33.6 (26.5)	52.1 (42.6)	42.2 (33.4)	63.8 (57.2)
[Fur+H] ⁺ -3.2	149.5 (106.5)	170.6 (127.6)	160.5 (117.0)	168.0 (121.9)
[Eum+JII+ 2 2	40.8 (33.5)	58.6 (49.1)	49.6 (40.8)	69.5 (62.7)
[Fur+H] ⁺ -3.3	156.7 (113.5)	177.1 (134.1)	168.2 (124.4)	173.7 (127.4)
1Eve 111+ 2-4	48.2 (40.7)	66.3 (56.7)	57.5 (48.2)	75.7 (68.6)
[Fur+H] ⁺ -3.4	164.1 (120.7)	184.8 (141.7)	175.8 (131.8)	179.9 (133.3)

^a Calculations performed at the stated level of theory using a 6-311+G(2d,2p) basis set with geometries calculated at B3LYP/6-311+G(d,p) level. Values are given relative to the lowest energy [Suc+H]⁺ structure at each level of theory. Gibbs energies in parentheses. Values in italics are given relative to the predicted GS of [AsnThr+H]⁺ at each level of theory and include NH₃. ^b Calculations performed at the B3LYP-GD3BJ/6-311+G(2d,2p)//B3LYP-GD3BJ/6-311+G(d,p) level. ^c [Suc+H]⁺-1.5 collapses to [Suc+H]⁺-1.2.

Table 4. Fitting Parameters of Equation 1, Threshold Energies at 0 K, and Entropies of Activation at 1000 K for Cross Sections of the Reactions Indicated^a

Product	TS	Frequency Scaling ^b	σ_0	n	E ₀ (eV)	$\Delta S^{\dagger}_{1000}$ (J/K mol)
m/z 216	TS _{O-OxaI-1}	1.00	12.4 (1.5)	1.0 (0.2)	1.14 (0.05)	-36 (0.3)
m/z 217	$TS_{N\text{-}Suc}$	0.77			1.45 (0.08)	37 (20) ^c
m/z 216	$TS_{O\text{-}OxaI\text{-}2}$	1.00	12.4 (1.5)	1.0 (0.1)	1.21 (0.05)	-20 (0.2)
m/z 217	$TS_{N\text{-}Suc}$	0.75			1.47 (0.06)	$47(11)^c$
m/z 216	TSo-oxaI-2	1.25	18.8 (3.0)	0.3 (0.1)	1.06 (0.05)	-91 (0.8) ^d
m/z 217	$TS_{N\text{-}Suc}$	1.00			1.27 (0.05)	-46 (0.5)
m/z 216	TS _{O-OxaI-2}	1.00	12.3 (1.3)	0.9 (0.1)	1.21 (0.05)	-20 (0.2)
m/z 217	$TS_{N\text{-}Fur}$	0.90			1.46 (0.06)	$33 (5)^e$
m/z 216	$TS_{O\text{-}OxaO}$	1.00	12.3 (1.4)	1.0 (0.1)	1.15 (0.05)	-25 (0.3)
m/z 217	$TS_{N\text{-}Suc}$	0.75			1.47 (0.07)	47 (11) ^c
m/z 216	TSo-oxao	1.00	12.5 (1.4)	1.0 (0.1)	1.16 (0.05)	-25 (0.3)
<i>m/z</i> 217	TS _{N-Fur}	0.90			1.47 (0.05)	33 (5) ^e

^a Uncertainties in parentheses. ^b Scaling factor applied to frequencies < 900 cm⁻¹. ^c Δ S[†]₁₀₀₀ without scaling is -46 J/K mol. ^d Δ S[†]₁₀₀₀ without scaling is -20 J/K mol. ^e Δ S[†]₁₀₀₀ without scaling is 1.2 J/K mol.

Table 5. Enthalpies and Gibbs Energies (kJ/mol) of Reaction at 0 and 298 K for Deamidation and Dehydration Reactions^a

Reaction	$\Delta { m H}_0{}^b$	$\Delta ext{H}_{298} ext{-}\Delta ext{H}_0{}^c$	ΔΗ298	$T\Delta S_{298}^{\ c}$	ΔG_{298}
Dehydration, TS _{O-Oxal-2}	117 (5)	0.4 (0.1)	117 (5)	-5.2 (0.2)	123 (5)
Deamidation, TS _{N-Suc}	142 (6)	9.3 (1.1)	151 (7)	9.0 (2.8)	142 (6)

^a Uncertainties in parentheses.

^b Experimental values from Table 4 for analysis with TS_{N-Suc} and TS_{O-Oxal-2}.

^c Calculated using standard formulae and molecular constants calculated at the B3LYP/6-311+G(d,p) level.

Table 6. Comparison of 0 K Reaction Energies for the Deamidation and Dehydration Processes of Asparaginyl Dipeptides

Reaction	Species	Experiment ^a	B3LYP ^b	B3LYP- GD3BJ ^c	B3P86 ^b	MP2(full) ^b
Succinimide	[AsnGly+H] ⁺	128 (7)	151	143	143	133
Formation	[AsnAla+H] ⁺		163	154	155	137
	[AsnVal+H] ⁺		172	163	164	145
	[AsnThr+H] ⁺	142 (6)	150 [136]	140 [120]	141 [127]	127 [105]
Furanone	[AsnGly+H] ⁺		132	148	140	143
Formation	[AsnAla+H] ⁺	123 (5)	132	145	139	134
	[AsnVal+H] ⁺	129 (5)	132	143	139	138
	[AsnThr+H] ⁺		137 [123]	149 [129]	145 [131]	143 [121]
Dehydration	[AsnGly+H] ⁺	117 (8)	127	117	130	111
	[AsnAla+H] ⁺	103 (6)	119	110	122	98
	[AsnVal+H] ⁺	114 (5)	116	110	118	103
	[AsnThr+H] ⁺	$117 (5)^d$	130 [116]	131 [111]	116 [102]	130 [107]
MADs^e			11 (7)	10 (8)	10 (7)	9 (4)

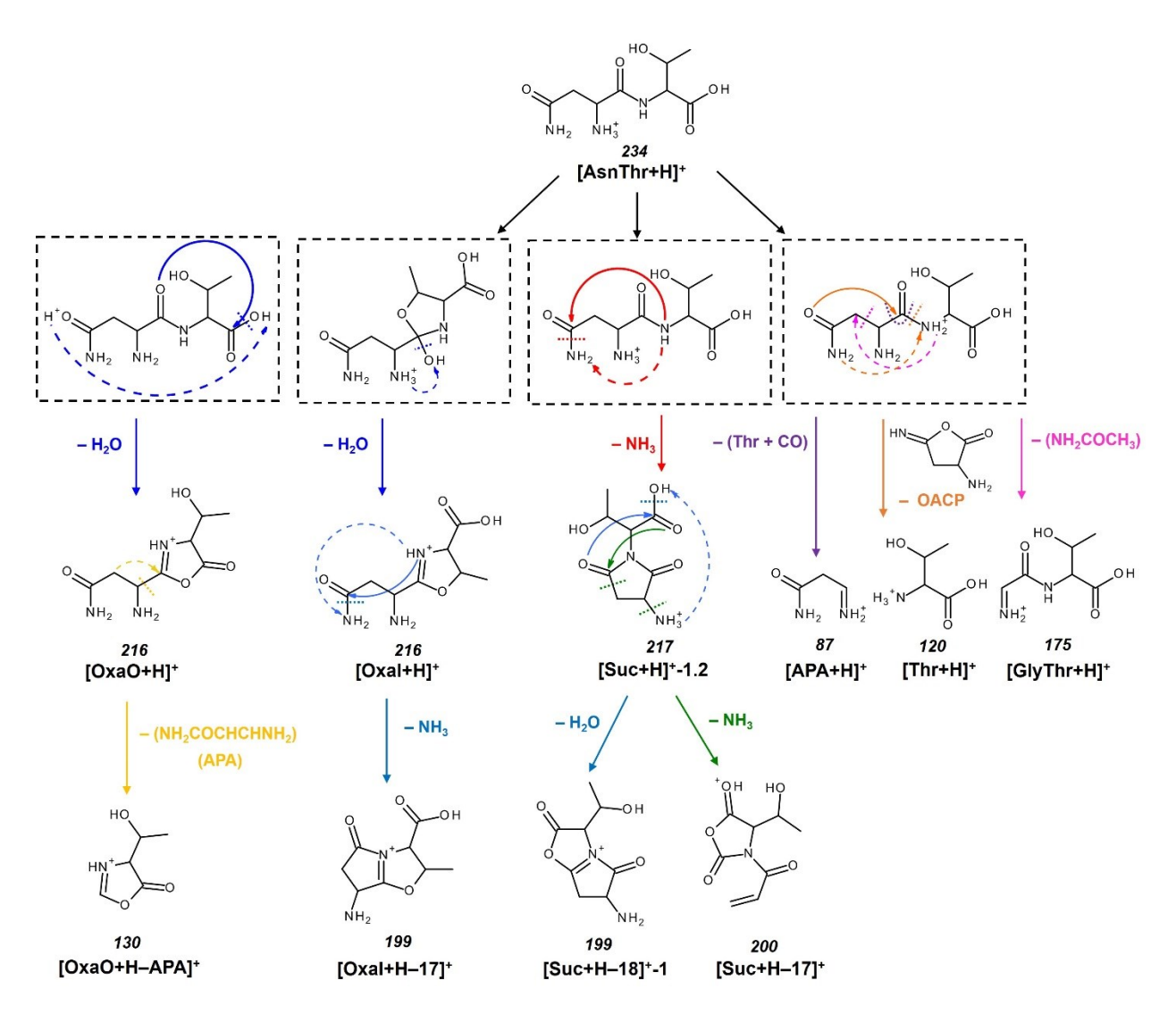
^a Experimental values from Table 4 and references 8, 10, and 11. Uncertainties in parentheses.

^b Calculations performed at the stated level of theory using a 6-311+G(2d,2p) basis set with geometries calculated at B3LYP/6-311+G(d,p) level, ZPE corrections included. Values in square brackets are given relative to the [N¹,CO^s,CO¹]-ttgtttt conformer.

^c Calculations performed at the B3LYP-GD3BJ/6-311+G(2d,2p)//B3LYP-GD3BJ/6-311+G(d,p) level of theory, ZPE corrections included.

^d Dehydration of [AsnThr+H]⁺ yields [OxaI+H]⁺ formation via TS_{O-OxaI-2} at threshold energies.

^e Calculated mean absolute deviations (MADs) between experiment and theory for observed deamidation and dehydration reactions using non-bracketed values for [AsnThr+H]⁺.



Scheme 1. Major decomposition reaction pathways for [AsnThr+H]⁺ observed in TCID studies under unit mass-resolution conditions. Numbers indicate mass-to-charge ratios and are given along with nomenclature used in the text. Dashed lines indicate proton movement, dotted lines indicate bond cleavages, solid lines indicate bond formation, and lines are color-coded to the resultant reaction.

Scheme 2. Possible nucleophilic attack rearrangements leading to the deami*d*ation (top two paths) or deami*n*ation (bottom path) of [AsnThr+H]⁺. Numbered atoms are used to indicate possible protonation sites for each product species.

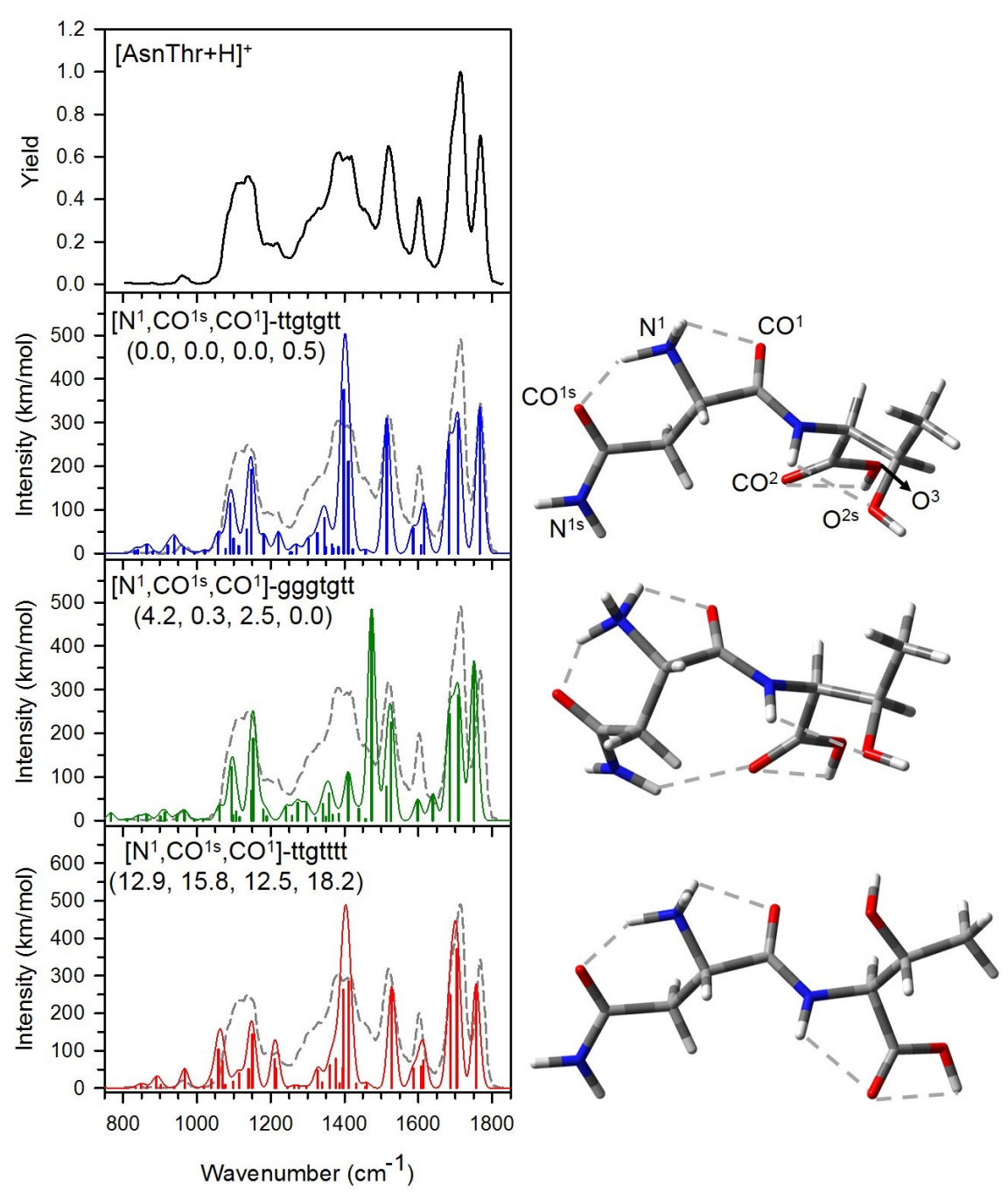


Figure 1. Experimental IRMPD spectrum of [AsnThr+H]⁺ (solid black and dashed grey traces) and calculated spectra for select low-energy conformers calculated at the B3LYP/6-311+G(d,p) level of theory. Relative 298 K Gibbs energies in kJ/mol are given at the B3LYP, B3LYP-GD3BJ, B3P86, and MP2(full) levels. Structures are shown to the right. Hydrogen bonds are indicated by dashed grey lines.

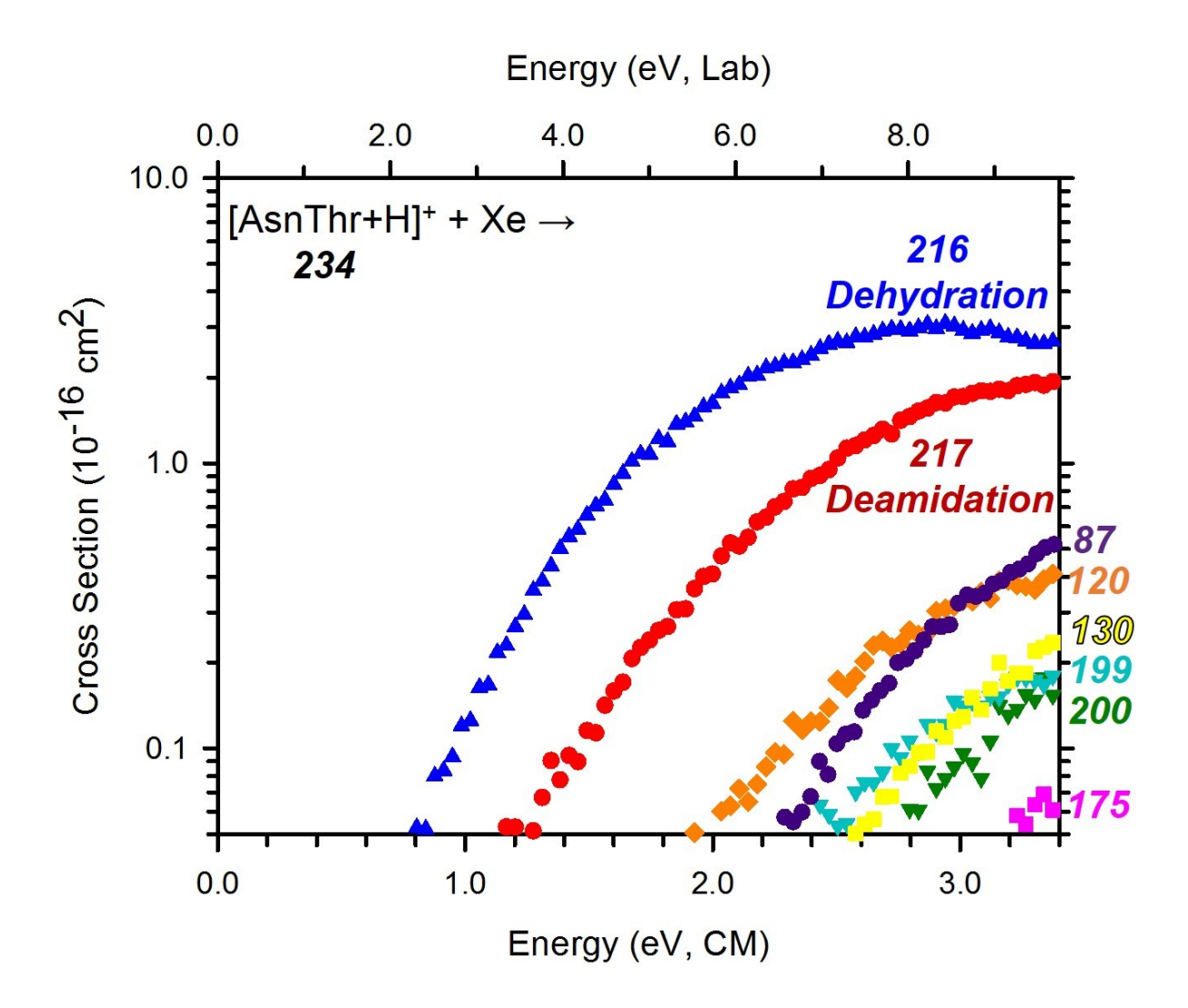


Figure 2. Cross sections for the collision-induced dissociation of [AsnThr+H]⁺ with Xe as a function of kinetic energy in the center-of-mass frame (lower x-axis) and laboratory frame (upper x-axis). Numbers indicate the mass-to-charge ratio of the ionic reaction products. Cross sections were measured at a Xe pressure of 0.3 mTorr.

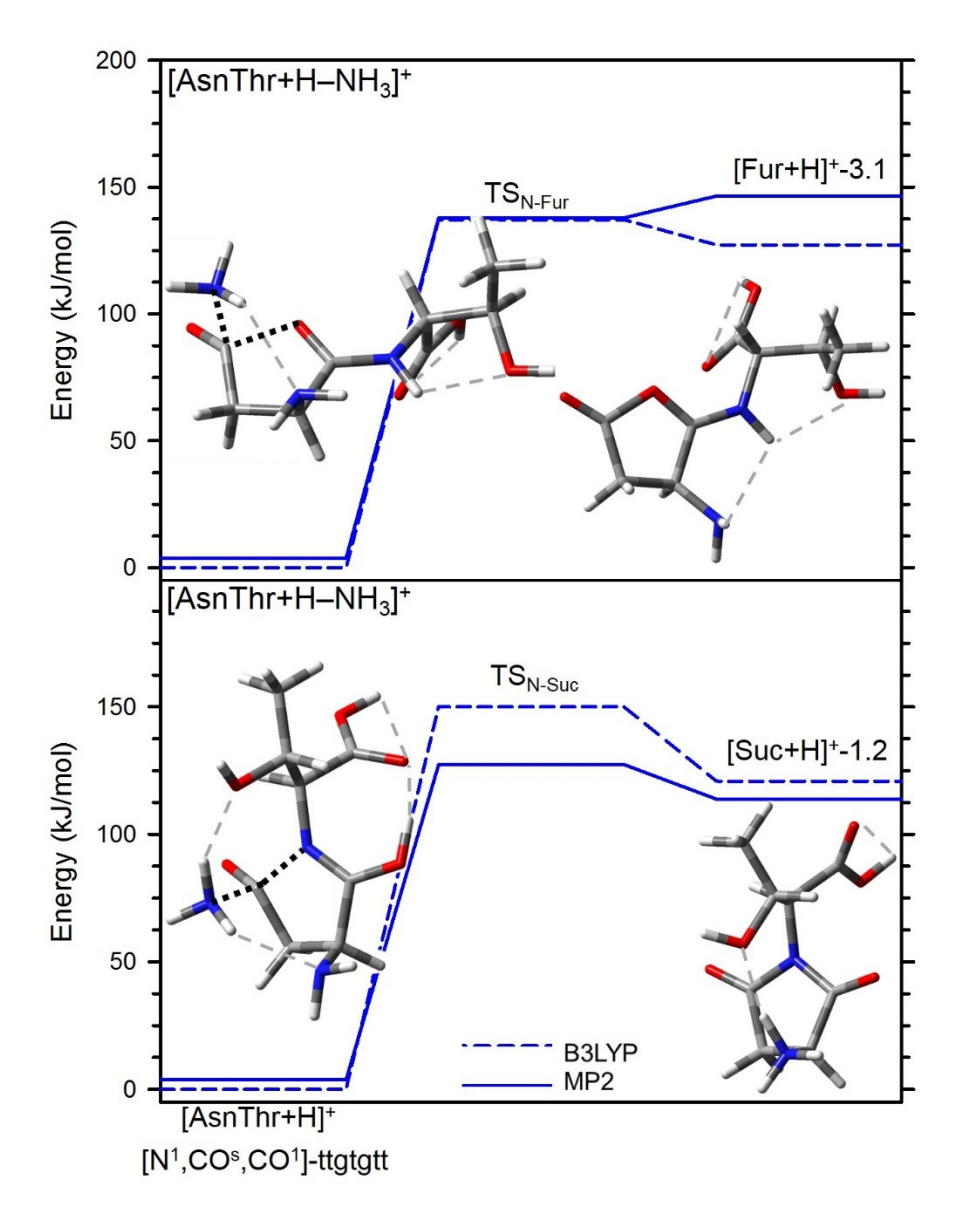


Figure 3. Simplified potential energy surfaces for deamidation. Relative single point energies at 0 K are taken from Table 1 and calculated at the B3LYP (dashed line) and MP2 (solid line) levels of theory. In the structures, which show the TS and products, hydrogen bonds are indicated by grey dashed lines and bond rupture and formation are designated by black dotted lines.

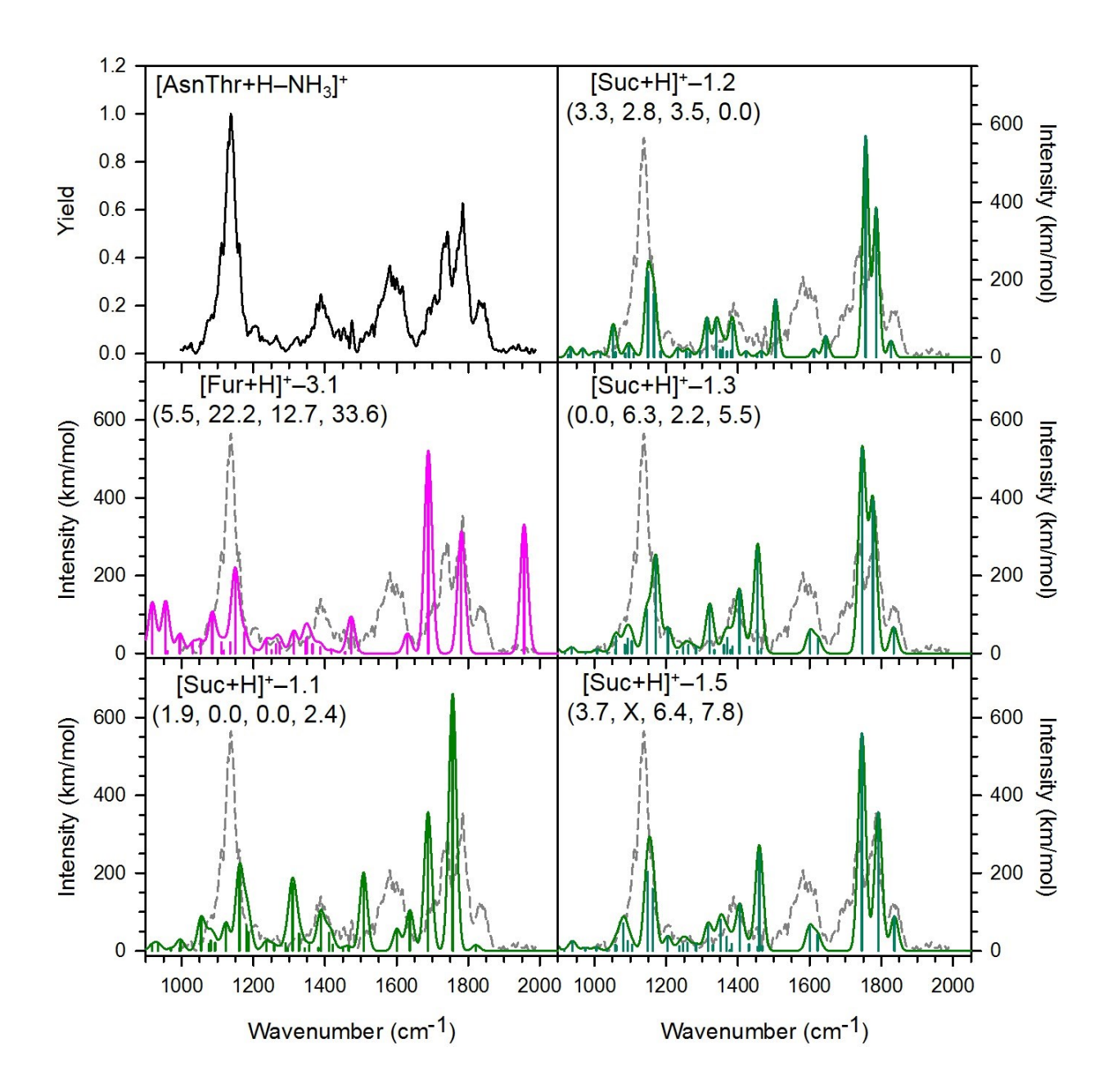


Figure 4. IRMPD spectra (solid black and dashed grey traces) of [AsnThr+H–NH₃]⁺ along with calculated spectra for select [Fur+H]⁺ (pink) and [Suc+H]⁺ (green) structures. Relative 298 K Gibbs energies (from Table 3) are given at the B3LYP, B3LYP-GD3BJ, B3P86, and MP2(full) levels.

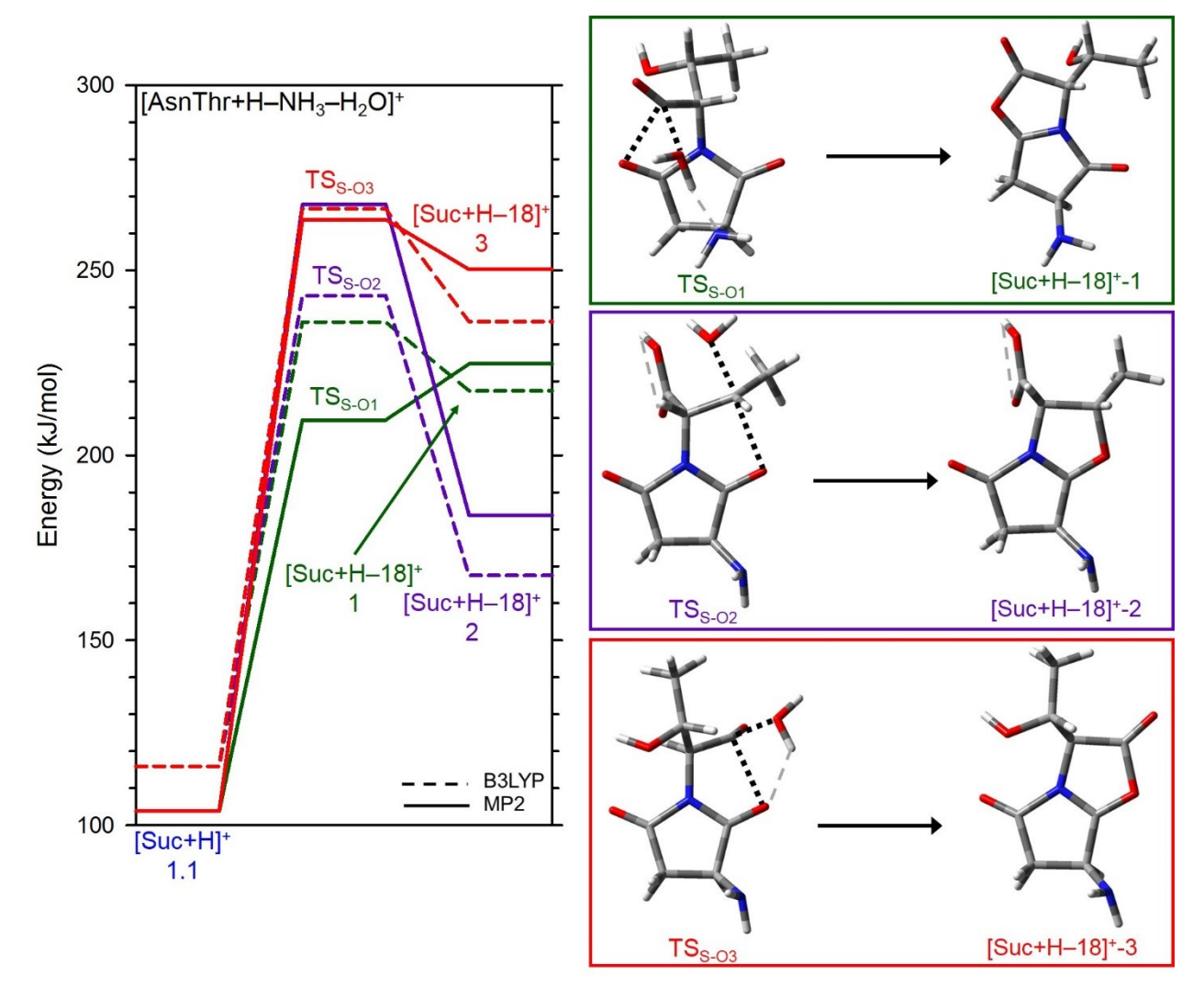


Figure 5. Simplified potential energy surfaces for the sequential dehydration of the succinimide deamidation product. Relative single point energies at 0 K are from Table 1 and calculated at the B3LYP (dashed lines) and MP2(full) (solid lines) levels. In the structures, hydrogen bonds are indicated by grey dashed lines and bond rupture and formation are designated by black dotted lines.

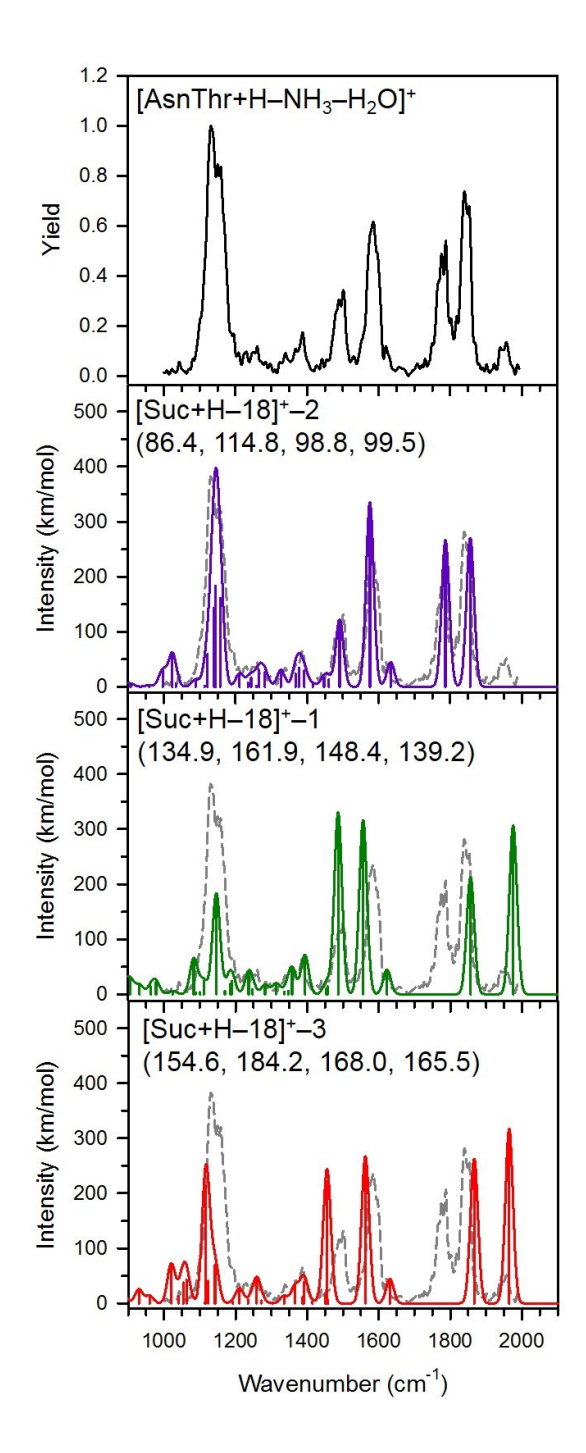


Figure 6. IRMPD spectra (solid black and dashed grey traces) of [AsnThr+H–NH₃–H₂O]⁺ along with calculated spectra for [Suc+H–18]⁺-1, 2, and 3. Relative 298 K Gibbs energies (from Table 1) are given at the B3LYP, B3LYP-GD3BJ, B3P86, and MP2(full) levels, respectively.

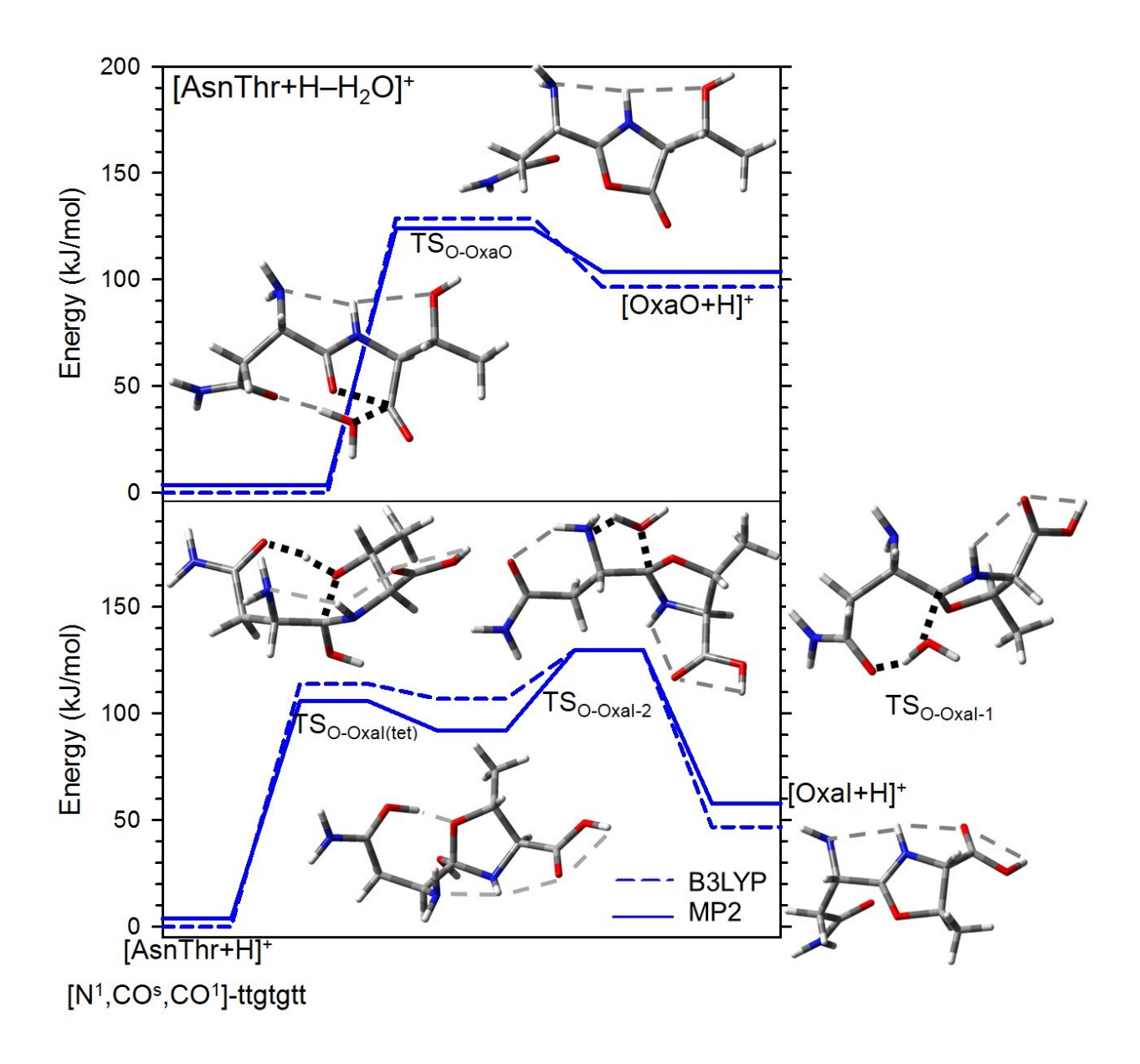


Figure 7. Simplified potential energy surfaces for [AsnThr+H]⁺ dehydration. Relative single point energies at 0 K are from Table 1 and calculated at the B3LYP (dashed lines) and MP2(full) (solid lines) levels. In the structures, which show the TS and products, hydrogen bonds < 2.7 Å are indicated by grey dashed lines and bond rupture and formation are designated by black dotted lines. The structure for an additional TS leading to $[OxaI+H]^+$ is given to the right.

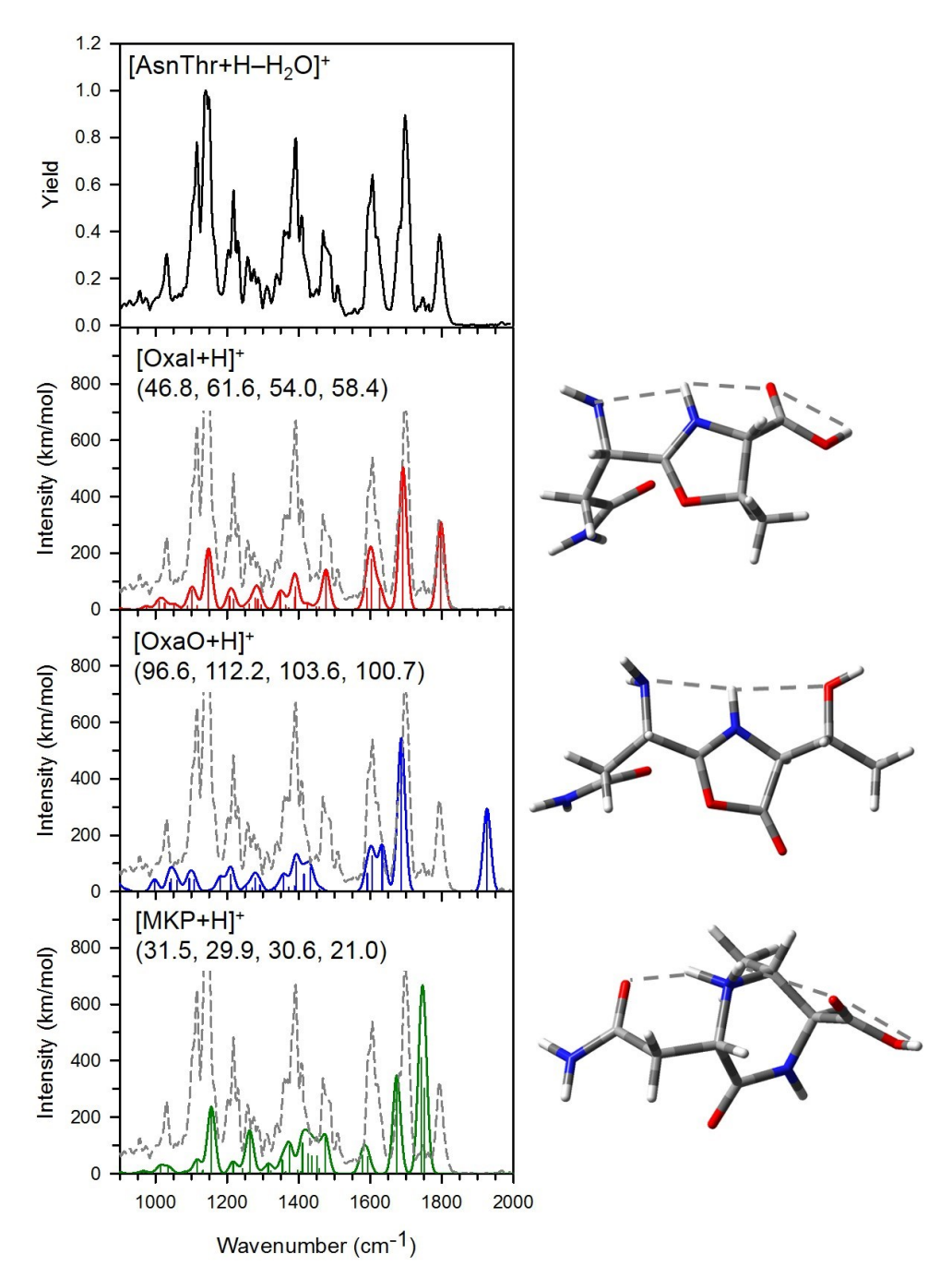


Figure 8. IRMPD spectra (solid black and dashed grey traces) of [AsnThr+H–H₂O]⁺ along with calculated spectra for ground structures of [OxaI+H]⁺, [OxaO+H]⁺, and [MKP+H]⁺. 0 K single point energies are given relative to the [AsnThr+H]⁺ GSs at the B3LYP, B3LYP-GD3BJ, B3P86, and MP2(full) levels, respectively.

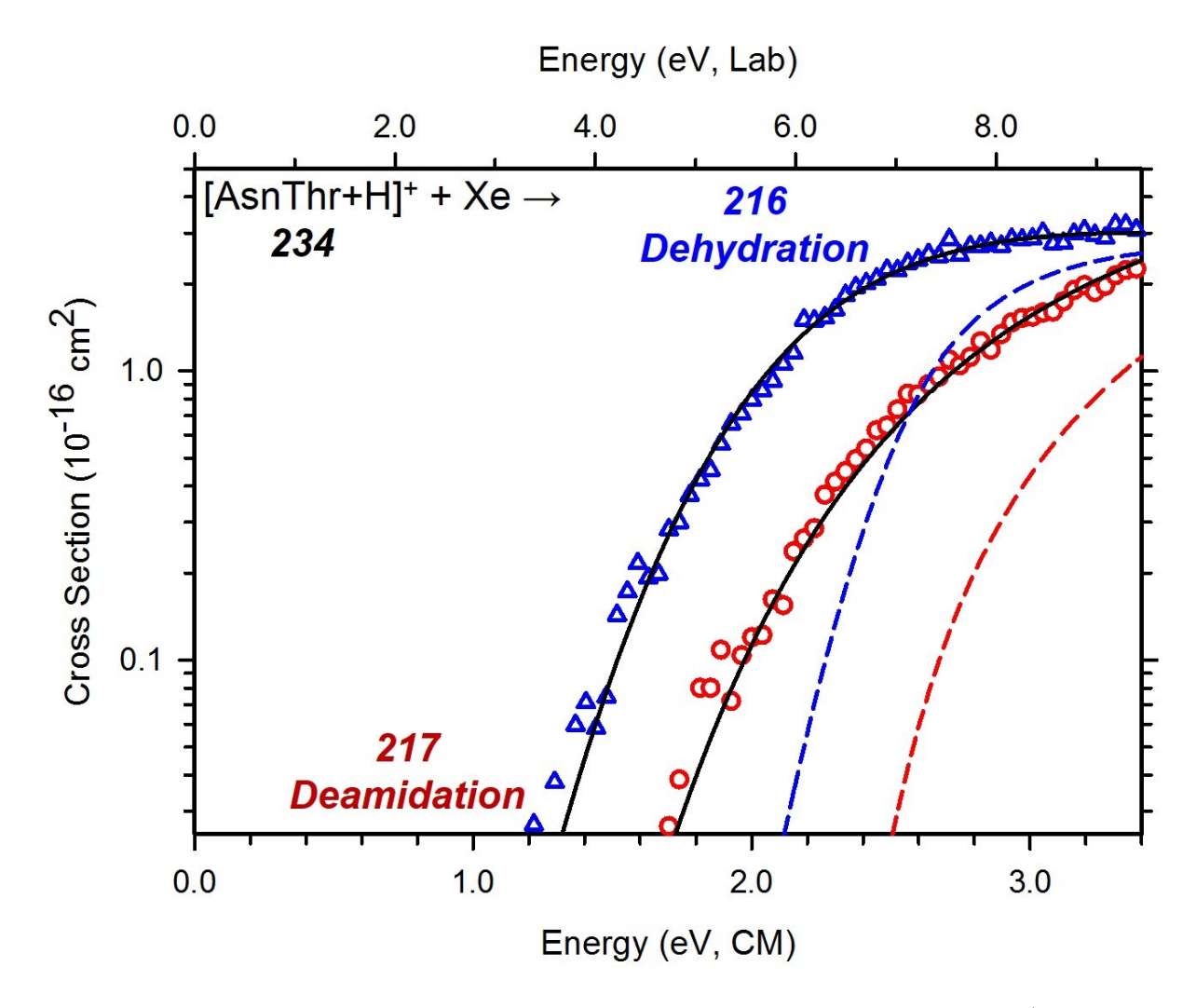


Figure 9. Cross section models of the main decomposition products of [AsnThr+H]⁺ as a function of collision energy with Xe in the center-of-mass frame (lower x-axis) and the laboratory frame (upper x-axis). Solid lines show the best fit to the data extrapolated to zero pressure (symbols), using the model of eq 1 convoluted over the neutral and ion kinetic and internal energy distributions. Dashed lines show the model cross sections in the absence of experimental kinetic energy broadening for reactants with an internal energy of 0 K. Data are modeled assuming succinimide formation via TS_{N-Suc} and dehydration via TS_{O-Oxal-2}.

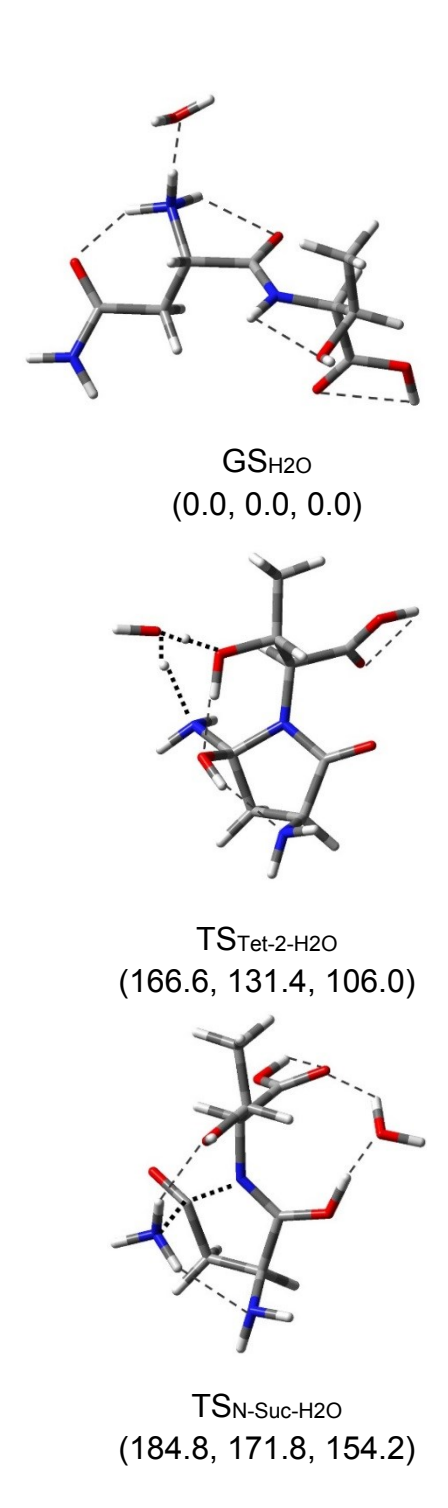
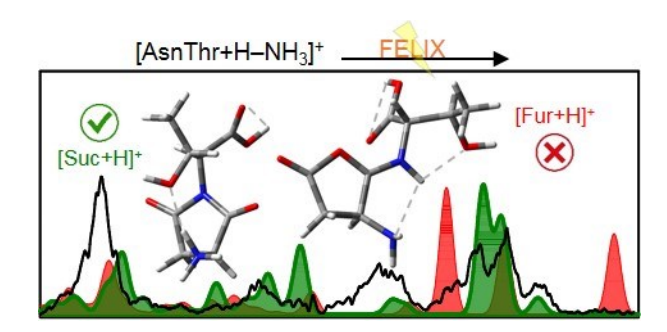


Figure 10. Solvated GS and TS species calculated for succinimide formation via the tetrahedral intermediate leading to [Suc+H]⁺-4.1 formation (via TS_{Tet-2-H2O}) and solvated succinimide formation yielding the experimentally observed [Suc+H]⁺-1.2 (via TS_{N-Suc-H2O}). Relative 0 K single point energies are given at the B3LYP, B3P86, and MP2(full) levels of theory.



TOC Graphic